Organization of cortical and thalamic input to inhibitory neurons in mouse motor cortex

Sandra U. Okoro[1], Roman U. Goz[1], Brigdet W. Njeri[1], Madhumita Harish[1], Catherine F. Ruff[1], Sarah E. Ross[1], Charles R. Gerfen[2], Bryan M. Hooks[1]

[1]University of Pittsburgh School of Medicine, Pittsburgh, Pennsylvania, USA
[2]National Institute of Mental Health, Bethesda, Maryland, USA

Correspondence: Dr. Bryan M. Hooks, 200 Lothrop Street BSTWR Suite W1458
Pittsburgh, PA 15213; 412-624-8465; hooksm@pitt.edu

ABSTRACT

Intracortical inhibition in motor cortex (M1) regulates movement and motor learning. If inhibitory cell types and cortical laminae targeted by cortical and thalamic afferents differ, then these afferents play different roles in regulating M1 output. We quantified input to two classes of M1 interneurons, parvalbumin+ (PV) fast-spiking cells and somatostatin+ (SOM) low-threshold-spiking cells, using monosynaptic rabies tracing. We then compared anatomical connectivity and functional connectivity based on synaptic strength from sensory cortex and thalamus. Functionally, each input innervated M1 interneurons with a unique laminar profile. Different interneuron types were excited in a distinct, complementary manner, suggesting feedforward inhibition proceeds selectively via distinct circuits. Specifically, somatosensory cortex (S1) inputs primarily targeted PV+ neurons in upper layers (L2/3) but SOM+ neurons in middle layers (L5). Somatosensory thalamus (PO) inputs targeted PV+ neurons in middle layers (L5). In contrast to sensory cortical areas, thalamic input to SOM+ neurons was equivalent to PV+ neurons. Thus, long-range excitatory inputs target inhibitory neurons in an area and cell type-specific manner which contrasts with input to neighboring pyramidal cells. In contrast to feedforward inhibition providing generic inhibitory tone in cortex, circuits are selectively organized to recruit inhibition matched to incoming excitatory circuits.

(Word count: 195)

INTRODUCTION

Motor cortex (M1) integrates long-range input from sensory cortex (S1) and thalamus to plan and control movement. Excitatory connectivity to excitatory neurons has been studied, but how different interneuron types are recruited by long-range input has received less attention. Cortical and thalamic sensory inputs arrive in M1, resulting in sensory activity (Ferezou et al., 2007; Hatsopoulos and Suminski, 2011; Huber et al., 2012; Murray and Keller, 2011), consistent with a role for M1 in active sensation (Hill et al., 2011) and sensorimotor learning (Asanuma, 1981). Input from S1 (Hoffer et al., 2003) excites pyramidal neurons primarily in upper layers of M1 (Kaneko et al., 1994a; Mao et al., 2011). Somatosensory input to M1 also originates from higher-order sensory thalamus, including the posterior nucleus (PO) (Deschenes et al., 1998; Harris et al., 2019; Ohno et al., 2012). These two classes of input (S1 and PO) both most strongly excited pyramidal neurons of L2/3 and L5A (Hooks, 2017; Hooks et al., 2013; Mao *et al.*, 2011). L2/3 and L5A neurons then provide descending input to pyramidal neurons in L5B that regulate movement (Anderson et al., 2010; Hooks et al., 2011; Kaneko et al., 1994b; Kiritani et al., 2012; Weiler et al., 2008).

A diverse range of cortical GABAergic interneuron types exist, playing an important role in regulating cortical excitation (Tremblay et al., 2016). Three major classes include parvalbumin-expressing (PV+), somatostatin-expressing (SOM+), and 5-HT3a receptor-expressing (5HT3aR+) interneurons (Lee et al., 2010). Of these, PV+ and SOM+ cells are found across the width of M1 from L2 to L6 (Fig. 1) (Lee *et al.*, 2010), while 5-HT3aR+ cells are restricted to the upper layers of cortex. PV+ interneurons include fast spiking interneurons, which target perisomatic regions of pyramidal neurons, and SOM+ interneurons, which include low threshold spiking interneurons (Cauli et al., 1997; Gibson et al., 1999; Kawaguchi and Kubota, 1997; Kubota, 2014). A subset of SOM+ interneurons, Martinotti cells, targets apical dendrites of pyramidal cells (Wang et al., 2004). Differences in subcellular targeting of excitatory cells contributes to different roles in regulating cortical output. Thus, understanding how different classes of interneuron are activated by distinct excitatory inputs is an important step in understanding how feedforward inhibition is recruited by different cortical afferents.

We tested whether the connectivity of long-range inputs to PV+ and SOM+ interneurons in M1 follows the pattern from sensory cortex studies. Because ascending thalamic inputs in sensory cortical areas principally target PV+ interneurons, we hypothesized that M1 PV+ interneurons would similarly be the major recipients of thalamic input. These conclusions are derived from studies of the connectivity of principal thalamic nuclei to cortical layer 4 (Cruikshank et al., 2007; Cruikshank et al., 2010), which is absent in M1. First, we quantified the

67 overall pattern of input to specific interneuron types using monosynaptic rabies tracing. Then,
68 because this method is not layer specific, we measured monosynaptic excitation to M1
69 interneurons functionally using channelrhodopsin-2 (ChR2)-assisted circuit mapping
70 (Cruikshank *et al.*, 2010; Petreanu et al., 2007; Petreanu et al., 2009) to assess synaptic input
71 strength as a function of laminar depth and specific interneuron type across layers in M1. In
72 contrast to the strong preference of thalamocortical input for PV+ interneurons in layer 4 of
73 sensory cortex (Cruikshank *et al.*, 2007; Cruikshank *et al.*, 2010), both methods found thalamic
74 input to SOM+ neurons that was nearly as strong as PV+ neuron input. The laminar pattern,
75 however, differed. Corticocortical afferents from S1 also targeted interneurons differently across
76 cell types: among PV+ neurons, L2/3 cells were most strongly excited, while for SOM+ neurons,
77 input arrived strongly in middle layers (L5). Furthermore, comparing inputs from S1 and
78 thalamus, PV+ neurons were targeted in a complementary fashion, with S1 exciting upper
79 layers (L2/3) and thalamus targeting middle layers (L5). Because S1 and PO targeted excitatory
80 neurons in similar layers (Hooks et al., 2015; Hooks *et al.*, 2013), the complementary pattern of
81 input to PV+ neurons suggests that feedforward inhibition does not simply silence cortex, but
82 integrates into local circuits in a specific fashion.

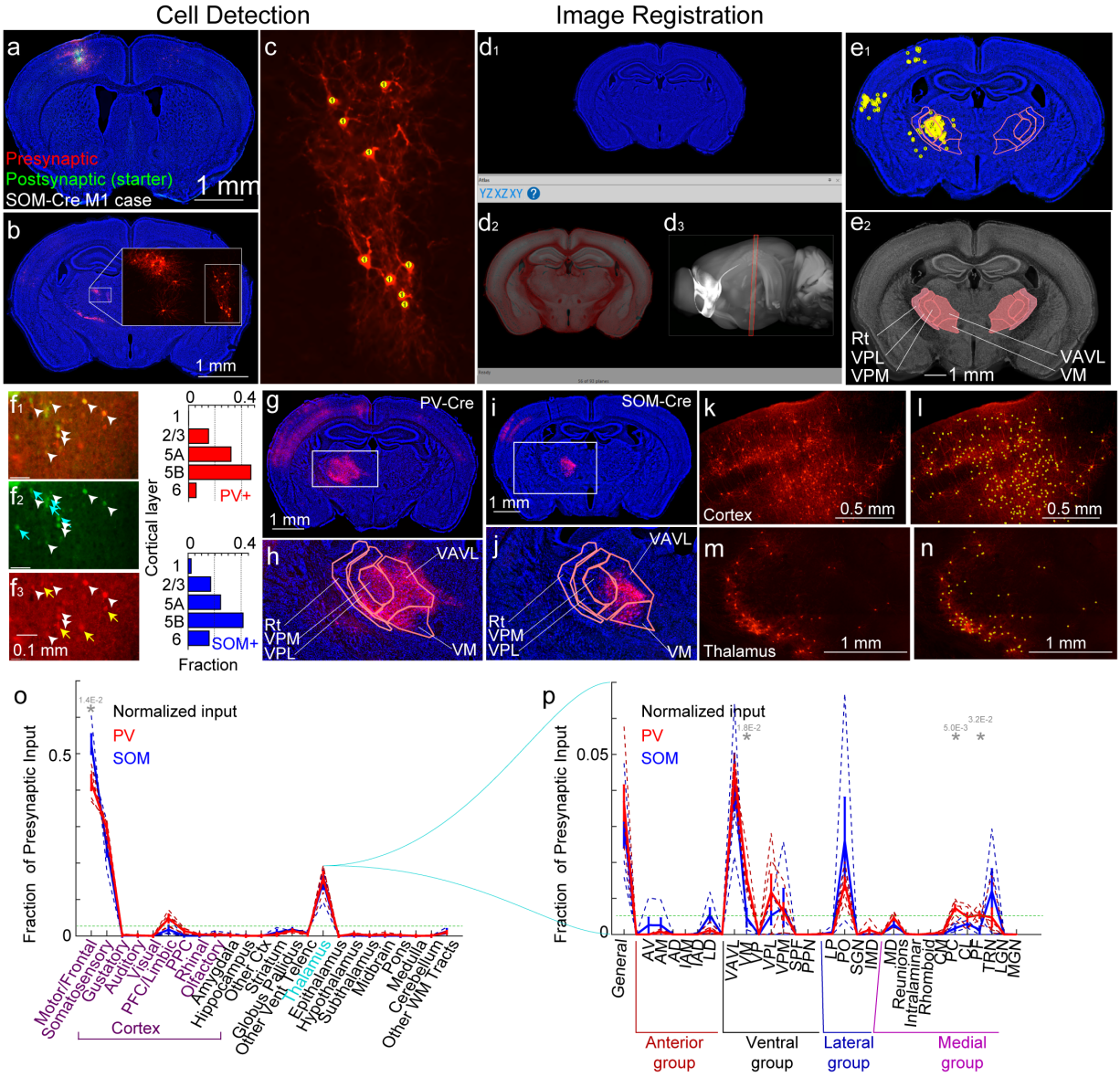

Figure 1 | Monosynaptic Retrograde Tracing of Inputs to Motor Cortex PV+ and SOM+ Neurons
(a) Injection site in M1 of a SOM-Cre mouse injected with AAV-DIO-TVA-RG-EGFP (green) and EnvA pseudotyped N2c RABV-tdTomato (red). Neurotrace Blue labels the tissue structure. (b) tdTomato-labeled thalamic neurons (inset). (c) tdTomato+ (red) somata detected in NeuroInfo. Markers are yellow. (d) Section registration in NeuroInfo. (d1) NeuroTrace Blue used as a structural marker in imaged sections. (d2-d3) Current reference section (teal, d2) and brain (black and white, d3) showing the reference atlas. The reference section (d2) can be aligned to the current section (d1; overlaid in red in d2) by adjusting the scale, or shifting and rotating the plane in which the reference brain is sectioned (control panel in e). The current plane orientation for the reference brain is shown as the red box in d3 (slightly offset from coronal). A nonlinear transform for each section is used to register each object in the current image to the reference brain coordinates. Detected neurons (from b-c) are then transformed to the reference atlas coordinate system. (e) Coronal sections showing the Allen CCF 3.0 and locations of S1 and motor and somatosensory thalamic nuclei (Rt, thalamic reticular nuc.; VAVL, ventroanterior/ventrolateral nuc.; VM, ventromedial nuc.; VPL, ventroposterolateral nuc.; VPM, ventroposteromedial nuc.). The positions of retrogradely labeled presynaptic neurons are marked with a yellow dot (top image) in an example SOM-Cre mouse injected in M1. Presynaptic neurons within ±0.1 mm of the plane are shown. The bottom image (e2) is labeled to indicate registered thalamic areas. (f) Injection site with starter cells in a SOM-Cre mouse. (f1) Merged image of green (f2) and red (f3) channels, showing yellow starter cells (white arrowheads in f1-f3) and singly labeled cells (blue arrows in f1 and yellow arrows in f3). (f2) Green, TVA+ neurons (putative starter cells); (f3) Red, tdTomato+ neurons (putative presynaptic neurons). Right, laminar distribution of PV+ and SOM+ somata, quantified as fraction of the total by layer. (g-h) Example section (g, expanded in h) showing retrograde label in S1 and thalamus from M1 starter cells in a PV-Cre mouse. Note S1 label and thalamic label. (i-j) Example section showing retrograde label in S1 and thalamus from M1 starter cells in a SOM-Cre mouse. Note S1 label and thalamic label. (k-n) Cell detection examples in a SOM-Cre mouse. In cortex (k), detected cell somata are labeled with yellow circles (l). Example images for thalamus (m-n). (o) Quantification of presynaptic neuron location from brains aligned to the Allen CCF V3.0. Fraction of the total presynaptic neuron population (±SEM) plotted for all M1 injections in PV-Cre (N=5, red) and SOM-Cre (N=4, blue) mice. Dashed lines represent individual cases; solid line represents mean. Green dashed line, threshold for testing. *, t-test p<0.05 (gray *, not significant when controlling for false discovery rate) (p) Quantification of thalamic inputs for all M1 injections in PV-Cre (N=5, red) and SOM-Cre (N=4, blue) mice. Data plotted as in (o), subdivided into distinct thalamic nuclei.

RESULTS

Anatomical tracing of long-range inputs to PV+ and SOM+ neurons

Incoming cortical and thalamic excitation to M1 directly excites pyramidal neurons (Hooks *et al.*, 2013; Mao *et al.*, 2011) and interneurons, evoking disynaptic feedforward inhibition. The interneurons carrying this feedforward inhibition likely include PV+ basket cells as well as SOM+ neurons. Conventional retrograde tracers can identify presynaptic cortical (Dum and Strick, 2002; Hoffer *et al.*, 2003; Reep et al., 1990; Rouiller et al., 1993) and thalamic inputs (Deschenes *et al.*, 1998; Kuramoto et al., 2009; Kuramoto et al., 2015; Ohno *et al.*, 2012) to M1 (Hooks *et al.*, 2013; Oh et al., 2014; Zingg et al., 2014), but do not differentiate between cell types in M1 receiving the input. To quantify how specific populations of interneurons are targeted by incoming cortical and thalamic afferents, we used genetically identified interneurons as starter cells for monosynaptic retrograde tracing with rabies virus (Callaway and Luo, 2015; Wickersham et al., 2007b). This enabled us to quantitatively compare presynaptic labeling across starter neuron types (PV+ and SOM+ neurons) as well as across cortical areas.

Using PV-Cre or SOM-Cre mice, we infected Cre+ interneurons with AAV-DIO-TVA-EGFP-B19G to label potential starter neurons and make them express both TVA receptor (to become infected with EnvA pseudotyped rabies virus) as well as the rabies coat protein B19G (Fig. 1f). The starter cells in these injections spanned cortical laminae (L2-6). After two weeks to express the receptor, EnvA-pseudotyped CVS-N2c G-deleted rabies expressing tdTomato (Reardon et al., 2016) was injected in forelimb motor cortex (fM1, N=5 for PV+, N=4 for SOM+ mice; see Table 1). Fixed brains were sectioned, immunoamplified, and imaged. The whole brain image stacks were reconstructed (Fig. 1a). Cell detection was then performed for tdTomato+ neurons in NeuroInfo (MBF Bioscience) in each plane using an artificial neural network (Fig. 1b-c; Supp. Fig. 1). The image stack was aligned to the Allen CCF V3.0 (Kuan et al., 2015; Oh *et al.*, 2014) using the structural label Neurotrace (blue, Fig. 1d-e), enabling the assignment of voxels containing structures and cells to defined cortical and thalamic regions (Fig. 1g-n; see Supp. Fig. 2 for detail of alignment in thalamus). fM1 was used to compare the data to results from the Brain Initiative Cell Census Network (BICCN) studies (Muñoz-Castaneda, 2020). This approach was limited since injections did not restrict starter PV+ or SOM+ neurons to a single cortical layer.

The distribution of presynaptic neurons was quantified by normalizing the number of cells detected in each brain region as a fraction of the total number of cells detected (Fig. 1o-p). The distributions were repeatable across different cases in the same brain region (Fig. 1o-p and Supp. Fig. 3), which indicated that the NeuroInfo alignment was effective across individual

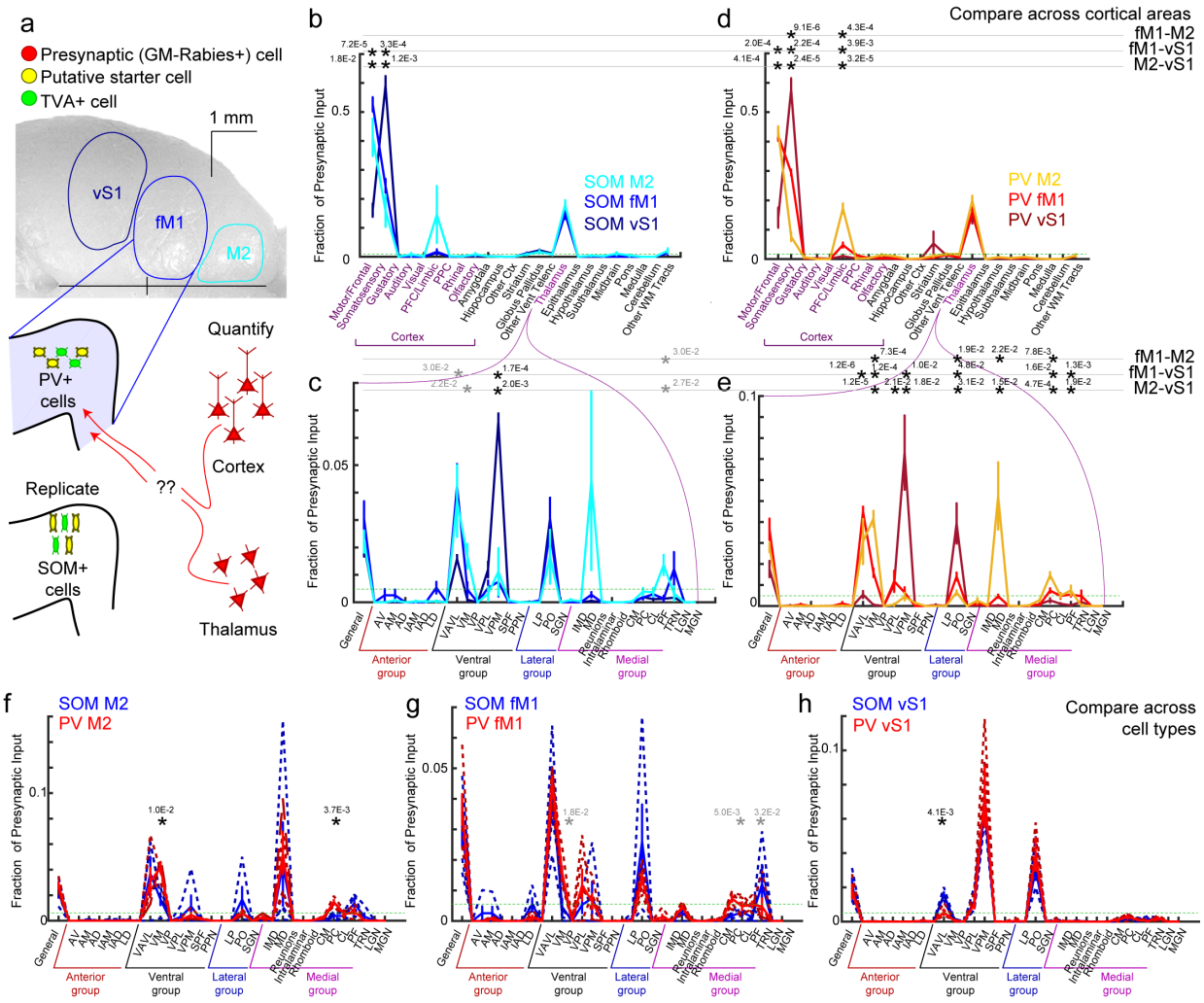

Figure 2 | Monosynaptic Retrograde Tracing of Inputs to PV+ and SOM+ Neurons Across Cortical Areas
(a) Schematic showing three dorsal cortical areas used for retrograde tracing from PV+ and SOM+ interneurons. In PV-Cre or SOM-Cre mice, injection of AAV expressing DIO-TVA-EGFP-B19G labels potential starter cells green in a Cre-dependent manner. This vector also expressed the TVA receptor to permit rabies uptake. Subsequent injection of EnvA-pseudotyped CVS-N2c-tdTomato rabies labels starter cells yellow (red+green), at left in cartoon and labels potential presynaptic partners red (at right in many cortical and thalamic areas). (b-c) Quantification of presynaptic neuron location for injections in SOM-Cre (N=4, M2; N=4, fM1; N=4, vS1; cool colors) mice. Whole brain image stacks were aligned to the Allen CCF V3.0. Presynaptic neuronal somata were detected and coordinates in CCF assigned to brain regions. Mean fraction of the total presynaptic neuron population (±SEM) plotted as in Fig. 1. Quantification of inputs to all brain regions (b) and to thalamic nuclei (c). (d-e) Data from injections in PV-Cre (N=4, M2; N=5, fM1; N=5, vS1; hot colors) plotted as in (b-c). (f-h) Data of (b-e) replotted to compare input to SOM+ (blue) and PV+ (red) neurons in the same cortical locations: M2 (f), fM1 (g), and vS1 (h). Dotted lines represent individual cases; solid lines represent mean. Green dashed horizontal lines in b-h represent threshold for statistical comparison. Black * represent significant differences (p value as indicated) after correcting for FDR. Gray * represent comparisons not significant after correction for FDR.

brains and that the retrograde tracing method was reliable. To minimize excessive comparisons, we limited comparisons to brain regions where at least one area exceeded a detection threshold (dotted line in Fig. 1o-p). Overall, the pattern was quite similar for inputs to PV+ and SOM+ neurons in M1. Most presynaptic inputs were found in cortex (Fig. 1o), in particular frontal and motor areas on the dorsal surface of cortex, as well as somatosensory cortex, which is strongly reciprocally connected to mouse M1 (Hooks, 2017; Mao *et al.*, 2011). About 20% of inputs for both interneuron classes were localized to thalamus, consistent with similar corticocortical and thalamocortical input to these cell types. We further examined the thalamocortical data by

128 subdividing labeled neurons by thalamic nuclei (Fig. 1p). Although the data showed that the
129 thalamic nuclei associated with M1 based on prior anatomic studies (Deschenes *et al.*, 1998;
130 Kuramoto *et al.*, 2009; Kuramoto *et al.*, 2015; Ohno *et al.*, 2012) were robustly represented,
131 including VAVL, VM, and PO, we did not detect significant differences between number of
132 neurons projecting to PV+ or SOM+ neurons. The ability to detect such differences was limited
133 by correction for false detection rate (Benjamini et al., 2009), with non-significant trends in VM
134 and two medial nuclei (PC and PF).
135 We extended the retrograde viral tracing study to two other cortical areas strongly
136 reciprocally connected with motor areas, primary somatosensory cortex and frontal cortex (M2).
137 Experimental procedures were identical, except for the targeting of viral injections to different
138 cortical areas in PV-Cre and SOM-Cre mouse lines. This gave a richer dataset for comparison.
139 We first made comparisons across cortical areas of starter cell within a given interneuron line
140 (Fig. 2b-d). For SOM+ neurons, the major areas labeled were motor cortex and frontal cortex
141 (greater in fM1 and M2 starter cases than in vS1 starter cases) and somatosensory cortex
142 (greater in vS1 starter cases), with a relatively uniform fraction of thalamic input (~20%) across
143 neocortical areas). PV+ input was similar, with the additional note of significantly greater input
144 from limbic areas (mostly orbital cortex) to M2 than to other areas. Comparison of input from
145 specific thalamic nuclei was considerably different across injection sites. In general, the pattern
146 of thalamic label could be used to infer the cortical target, with a reasonably large number of
147 nuclei providing a specific pattern of cortical input. For example, in cases using PV+ starter
148 neurons, vS1 injections could be identified by more robust VPM and PO labeling. fM1 injections
149 had strong input from VAVL and VM as well as PO and midline nuclei. M2 input was similar to
150 fM1 in receiving strong VAVL and VM input, but also received significant MD input (which vS1
151 and fM1 did not) as well as input from midline nuclei including PC and PF. This is consistent
152 with substantial differences in thalamocortical targeting across cortical areas. However, in
153 comparing input to different cell types within a given cortical area, few significant differences
154 were detected. For M2, PV+ interneurons labeled more thalamic cells in VM and PC compared
155 to SOM+ neurons in M2. In vS1, SOM+ interneurons labeled more VAVL neurons than PV+
156 neurons. For most nuclei, there were no detectable differences. In general, this was consistent
157 with much larger differences in thalamic label for cortical areas than for specific cell types within
158 a cortical area.
159

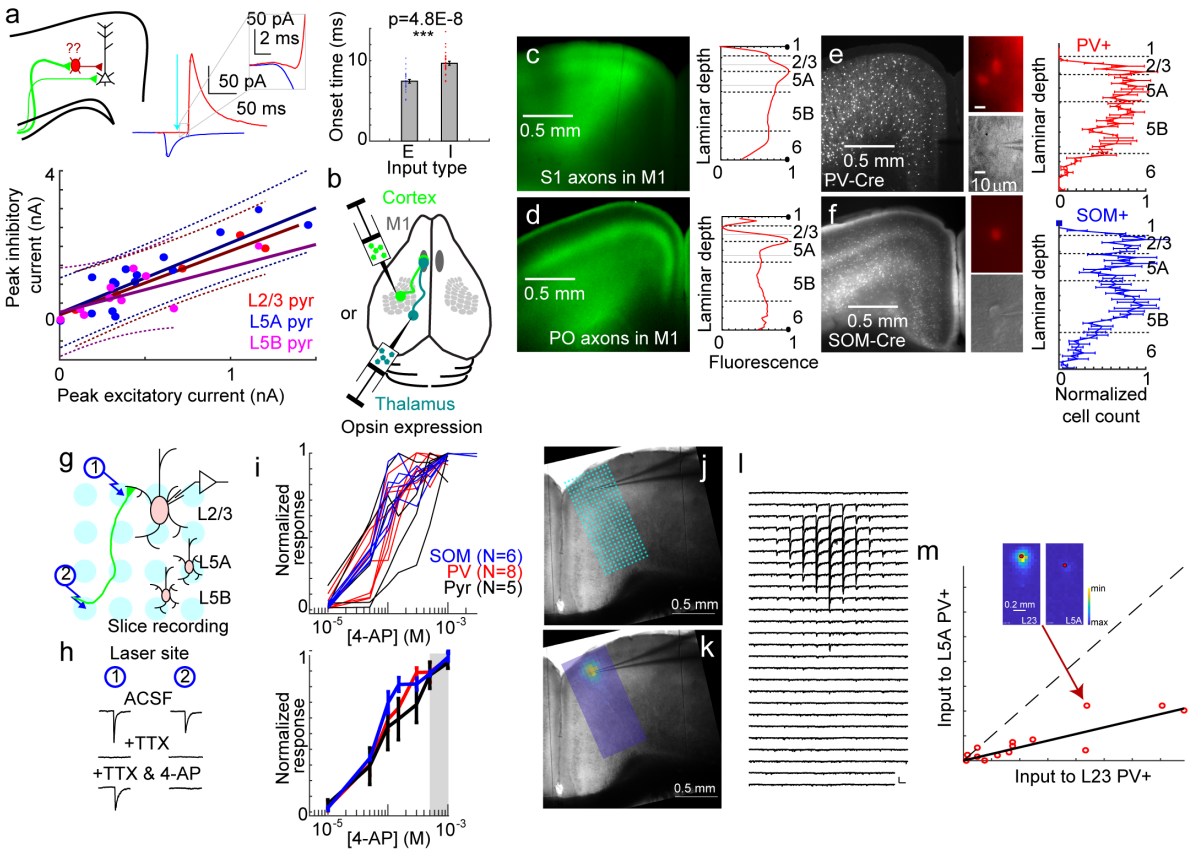

Figure 3 | Mapping long-range excitatory inputs to mouse motor cortex interneurons
(a) Interneurons carry feedforward inhibition in M1. Whole-cell recordings at -70 mV (blue) and 0mV (red) show optically induced feedforward inhibition from S1 inputs to M1 (bottom left) with a short latency difference (inset). Difference in latency between EPSC (blue) and IPSC (red) is plotted to compare onset (mean and SE; N=29). EPSC and IPSC amplitude are roughly proportional (right) across all cortical layers (bottom right). Linear fit and 95% confidence interval (dashed lines) plotted. (b) AAV vectors expressing optogenetic activators (ChR2 or Chronos) were stereotaxically injected into cortex (S1, light green) or thalamus (PO, dark green). (c) mVenus+ axons from S1 arborize across layers of M1 in a columnar projection (left, 4x image). Fluorescence is highest in L5A (right, brightness quantified across cortical layers). (d) mVenus+ axons from PO arborize across layers of M1 in two main layers (left). Fluorescence is highest in L1 and L5A (right). (e) PV-Cre mice were crossed to a tdTomato reporter (Ai14), labeling interneurons across M1 in L2-6. Postsynaptic interneurons were recorded across all layers for comparison. Inset (60x, fluorescence image, top, and corresponding brightfield image, bottom) shows patch pipette on tdTomato+ neuron in PV-Cre x Ai14 mouse. Normalized laminar distribution of PV+ somata (N=5 slices) measured at right. (f) SOM-Cre mice were crossed to a tdTomato reporter (Ai14), labeling interneurons across M1 in L2-6. L1 signal represents tdTomato+ axons from SOM+ neurons. Postsynaptic interneurons were recorded across all layers for comparison. Normalized laminar distribution of SOM+ somata (N=5 slices) measured at right. (g) Targeted whole cell recordings in brainslice were made from interneurons while stimulating with a 470nm laser at different points, shown in light blue. Full grid illustrated as in (j). (h) 470nm stimulation excites axons at example points 1 & 2, but TTX addition extinguishes responses. Addition of 4-AP permits local release at points where opsin+ axons contact interneuron dendrites (Point 1) but not distant points along the axon (Point 2). (i) Similar concentrations of 4-AP are required to restore synaptic responses regardless of postsynaptic neuron type (Pyr = pyramidal neuron). Individual cells plotted at top; average and SE plotted at bottom. Grey box represents [4-AP] used for mapping. (j) Typical input mapping experiments sampled a 12x26 point grid with points spaced at 50 mm and aligned to the pia. Brightfield image (4x) shows recording pipette in M1. (k) Heatmap shows stronger responses (red) near the soma of the recorded neuron. (l) Example traces for a L2/3 PV+ neuron show location of input. (m) Inset shows two maps to compare input between L2/3 and L5A PV+ interneurons. The summed synaptic input across the map is compared for each cell pair recorded in the same slice. Arrow indicates a point from one L2/3-L5A pair. Dashed line represents y=x (similar input to both layers); solid line represents the geometric mean of the L2/3 and L5A input strength, presented as a line of equivalent slope.

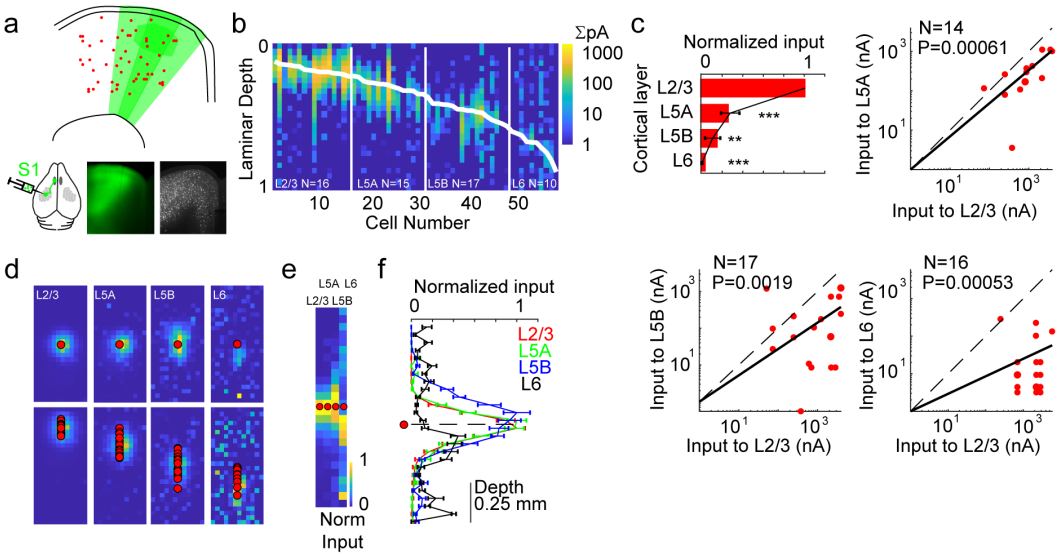

Figure 4 | S1 input to M1 targets upper layer PV+ neurons
(a) Cartoon showing PV+ neurons (red) in GFP+ axons from S1. (b) S1 input to M1 PV+ neurons across layers (N=58 total). Each cell is represented as a single column (vector), with the rows of the input mapped summed and aligned to the pia. Diagonal white line represents the soma location for that cell. Vertical white lines represent layer divisions. Synaptic strength (summed, in nA) for each location in depth are represented by the heatmap (scale at right). Laminar depth is normalized to 0=pia, 1=white matter. (c) Strength of synaptic input. The bar represents the geometric means of the amplitude ratio, normalized to the layer receiving the strongest input (L23). The overlaid graph shows the mean ratio and SD (based on 10000 replicate bootstrap). Adjacent to the summary, three graphs for comparison of input strength across neurons in different cortical layers. Each point represents input to a pair of neurons in the same slice (circle for each neuron). Dashed line represents unity. N, Number of pairs; p value, Wilcoxon signed rank test. (d) Maps of synaptic input location in the dendritic arbor for PV+ neurons in each layer. Top row, normalized soma-centered map (maps registered to soma center across cells). Bottom row, normalized pia-aligned maps. Normalized maps are noisy when input is weak. (e,f) Input location summarized for all four layers. Normalized mean input maps were averaged into a vector (e) and aligned to the soma (red circle). These were graphed with mean and SD (f), showing input relative to the soma in 50 μm bins. Dashed line indicates soma depth. *=p<0.05, **=p<0.01, and ***=p<0.001.

M1 directly excites pyramidal neurons (Hooks *et al.*, 2013; Mao *et al.*, 2011). Our data showed that these inputs were capable of evoking disynaptic feedforward inhibition by recording from pyramidal neurons in M1 in brain slice while exciting ChR2+ axons from S1 at -70 mV and +0 mV and quantifying the EPSC and IPSC amplitude, respectively (Fig. 3). The feedforward inhibition at +0 mV onset ~2 ms slower than the excitation (Fig. 3a). Across M1 layers, excitation is matched to inhibition, with similar ratios across layers. The interneurons carrying this feedforward inhibition are unknown, but are presumed to include PV+ basket cells. Further, it is likely that the GABAergic neurons carrying the disynaptic inhibition reside mainly in the same layer as the pyramidal neuron soma (Katzel et al., 2011). To identify the source of this disynaptic inhibition, we then quantified how specific populations of interneurons are targeted by incoming cortical and thalamic afferents. This experiment will also permit a direct comparison of functional synaptic connectivity by synaptic circuit mapping and anatomical tracing by retrograde viruses. We labeled axons from S1 or PO with ChR2-mVenus. These axons arborized in distinct layers of cortex (Fig. 3c-d). We selected two populations of Cre-driver mice (PV-Cre and SOM-Cre) crossed to a tdTomato reporter (Ai14) (Madisen et al., 2010) in order to label genetically defined interneurons across the thickness of M1. We then targeted whole-

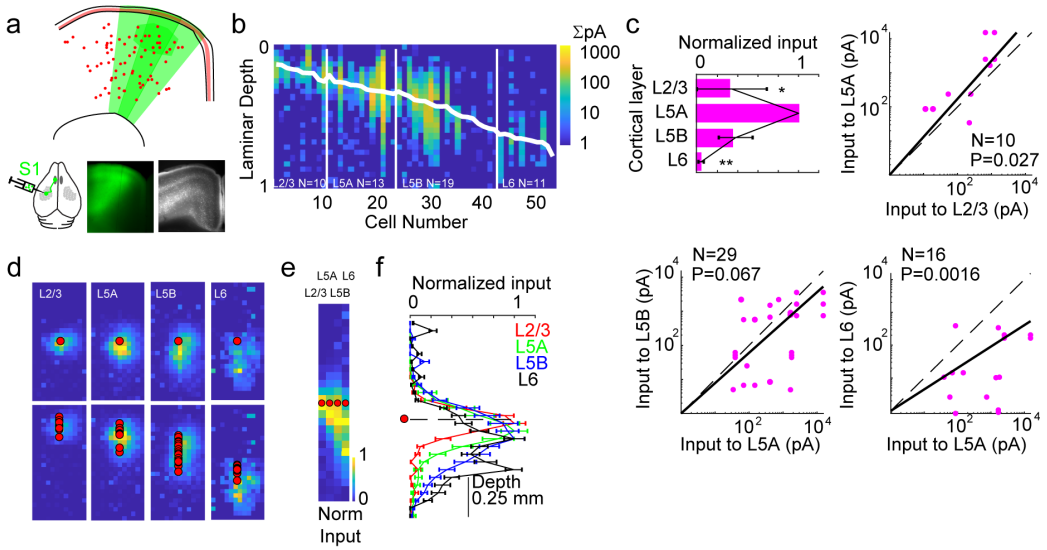

Figure 5 | S1 input to M1 targets middle layer SOM+ neurons
(a) Cartoon showing SOM+ neurons (red) in GFP+ axons from S1. (b) S1 input to SOM+ neurons across layers (N=53 total). Each cell is represented as a single column (vector), with the rows of the input mapped summed and aligned to the pia. Diagonal white line represents the soma location for that cell. Vertical white lines represent layer divisions. Synaptic strength (summed, in nA) for each location in depth are represented by the heatmap (scale at right). Laminar depth is normalized to 0=pia, 1=white matter. (c) Strength of synaptic input. The bar represents the geometric means of the amplitude ratio, normalized to the layer receiving the strongest input (L5A). The overlaid graph shows the mean ratio and SD (based on 10000 replicate bootstrap). Adjacent to the summary, three graphs for comparison of input strength across neurons in different cortical layers. Each point represents input to a pair of neurons in the same slice (circle for each neuron). Dashed line represents unity. N, Number of pairs; p value, Wilcoxon signed rank test. (d) Maps of synaptic input location in the dendritic arbor for SOM+ neurons in each layer. Top row, normalized soma-centered map (maps registered to soma center across cells). Bottom row, normalized pia-aligned maps. Normalized maps are noisy when input is weak. (e,f) Input location summarized for all four layers. Normalized mean input maps were averaged into a vector (e) and aligned to the soma (red circle). These were graphed with mean and SD (f), showing input relative to the soma in 50 μm bins. Dashed line indicates soma depth.

cell recordings to tdTomato+ interneurons in M1 brain slices in the field of mVenus+ axon terminals. We used a 470 nm light to excite ChR2+ axon terminals while recording in TTX, CPP, and 4-AP (sCRACM) (Petreanu *et al.*, 2007; Petreanu *et al.*, 2009). TTX prohibited action potentials, ensuring inputs measured were monosynaptic. 4-AP slowed axon repolarization, allowing the ChR2-evoked EPSC to occur (Fig. 3g-h). Because we were concerned that axons targeting different cell types might vary in their responsiveness to 4-AP, we confirmed that addition of 4-AP in the presence of TTX restored synaptic release with similar effectiveness. In mapping experiments, a single interneuron was recorded while stimulating the brain slice with a 470 nm laser. A 12x26 grid (Fig 3j) was used for stimulation, resulting in evoked EPSCs (Fig. 3l) that differed in amplitude depending on the location of the laser stimulus. A heat map showing the size of the response was then plotted on top of the cell location in the slice (Fig. 3k). We compared each pair of interneurons in different layers recorded in the same slice, summing the EPSC amplitude across the map. This measure of input strength was used to compare EPSC amplitude across layers (Fig. 3m). Thus, our comparisons of input strength (Fig. 4-7) required pairwise comparison of neurons recorded in

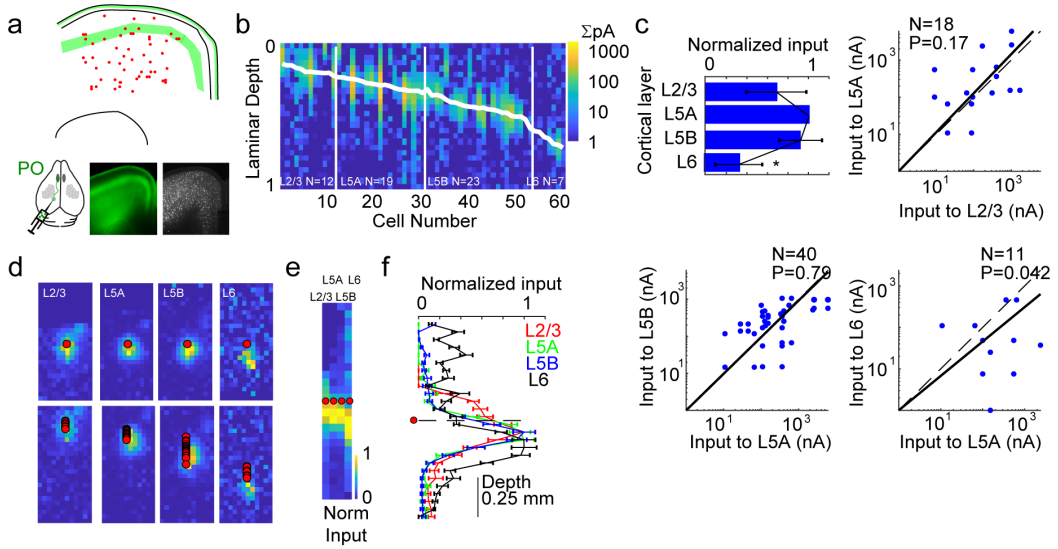

Figure 6 | PO input to M1 PV+ neurons targets upper and middle layers
(a) Cartoon showing PV+ neurons (red) in GFP+ axons from PO. (b) PO input to PV+ neurons across layers (N=61 total). Each cell is represented as a single column (vector), with the rows of the input mapped summed and aligned to the pia. Diagonal white line represents the soma location for that cell. Vertical white lines represent layer divisions. Synaptic strength (summed, in nA) for each location in depth are represented by the heatmap (scale at right). Laminar depth is normalized to 0=pia, 1=white matter. (c) Strength of synaptic input. The bar represents the geometric means of the amplitude ratio, normalized to the layer receiving the strongest input (L5A). The overlaid graph shows the mean ratio and SD (based on 10000 replicate bootstrap). Adjacent to the summary, three graphs for comparison of input strength across neurons in different cortical layers. Each point represents input to a pair of neurons in the same slice (circle for each neuron). Dashed line represents unity. N, Number of pairs; p value, Wilcoxon signed rank test. (d) Maps of synaptic input location in the dendritic arbor for PV+ neurons in each layer. Top row, normalized soma-centered map (maps registered to soma center across cells). Bottom row, normalized pia-aligned maps. Normalized maps are noisy when input is weak. (e,f) Input location summarized for all four layers. Normalized mean input maps were averaged into a vector (e) and aligned to the soma (red circle). These were graphed with mean and SD (f), showing input relative to the soma in 50 μm bins. Dashed line indicates soma depth.

the same slice to normalize for ChR2 expression between animals, and nonparametric statistics were used to avoid assumptions about the distribution of connection strength.

S1 targeting of PV+ and SOM+ interneurons in M1

First, we recorded from tdTomato+ PV+ interneurons in the whisker region of M1 in PV-Cre x Ai14 mice. S1 inputs to M1 mainly targeted PV+ interneurons in L2/3. L2/3 PV+ neurons received more than twice as much input than any other layer. All PV+ neurons (N=58) in all layers were plotted for comparison (Fig. 4b), with each map reduced to a column vector by summing the input map across rows. Most responsive cells and the strongest responding cells were found in L2/3. A pairwise comparison of L2/3 with other PV+ neurons recorded in the same slice showed that L5A neurons received only about 30% the input of L2/3 PV+ neurons ($P<0.001$). Similarly, input to L5B and L6 was even weaker (Fig. 4c). This input was mostly centered around the interneuron soma, as shown in maps where the grid is aligned to the soma (Fig. 4d-e). For layers with weaker input, noise is increased in normalized input maps (for example, L6 in Fig. 4d).

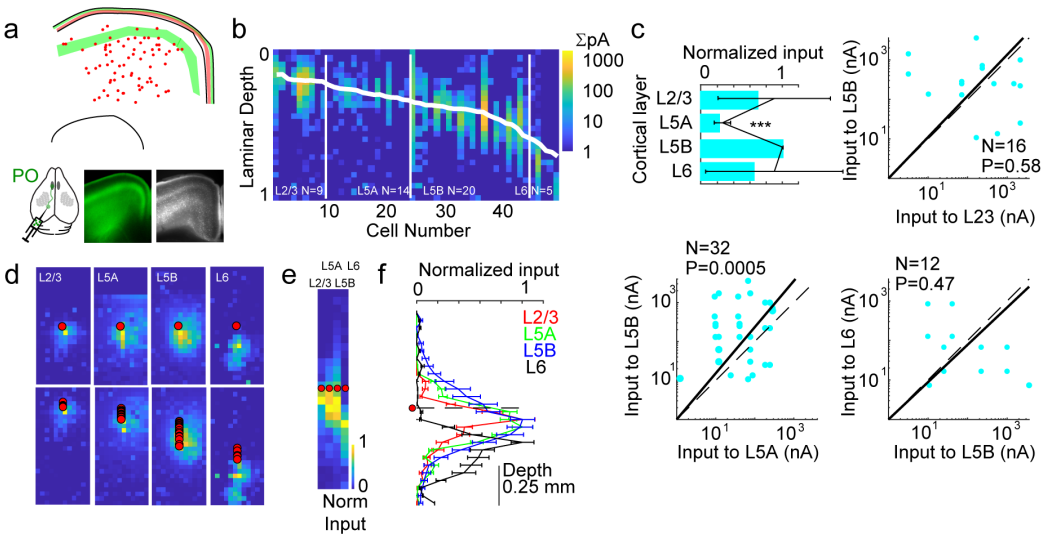

Figure 7 | PO input to M1 SOM+ neurons is variable
(a) Cartoon showing SOM+ neurons (red) in GFP+ axons from PO. (b) PO input to SOM+ neurons across layers (N=48 total). Each cell is represented as a single column (vector), with the rows of the input mapped summed and aligned to the pia. Diagonal white line represents the soma location for that cell. Vertical white lines represent layer divisions. Synaptic strength (summed, in nA) for each location in depth are represented by the heatmap (scale at right). Laminar depth is normalized to 0=pia, 1=white matter. (c) Strength of synaptic input. The bar represents the geometric means of the amplitude ratio, normalized to the layer receiving the strongest input (L5B). The overlaid graph shows the mean ratio and SD (based on 10000 replicate bootstrap). Adjacent to the summary, three graphs for comparison of input strength across neurons in different cortical layers. Each point represents input to a pair of neurons in the same slice (circle for each neuron). Dashed line represents unity. N, Number of pairs; p value, Wilcoxon signed rank test. Plots show substantial heterogeneity. (d) Maps of synaptic input location in the dendritic arbor for SOM+ neurons in each layer. Top row, normalized soma-centered map (maps registered to soma center across cells). Bottom row, normalized pia-aligned maps. Normalized maps are noisy when input is weak. (e,f) Input location summarized for all four layers. Normalized mean input maps were averaged into a vector (e) and aligned to the soma (red circle). These were graphed with mean and SD (f), showing input relative to the soma in 50 μm bins. Dashed line indicates soma depth.

We repeated this experiment for S1 inputs to SOM+ interneurons, using SOM-Cre x Ai14 mice (Fig. 5). As in PV-Cre mice, SOM-Cre labeled interneurons across the cortical thickness, allowing a fair comparison of input strength across layers. Here, S1 inputs most strongly targeted L5A interneurons. L2/3 SOM+ neurons only received about 30% the input of L5A SOM+ cells (Fig. 5c, $p<0.05$). L5B was not significantly weaker. L6 SOM+ neurons received the least input ($p<0.01$). As with PV+ neurons, S1 input was generally perisomatic, especially for L2/3 SOM+ cells. However, the center of mass of the input was shifted below the soma towards white matter for SOM+ cells in L5A, 5B, and 6 (Fig. 5d-f), suggesting that S1 axons were capable of targeting different subcellular domains in different interneuron types.

PO targeting of PV+ and SOM+ interneurons in M1

Next, we repeated these experiments while labeling thalamic inputs from PO nucleus of thalamus, a higher order somatosensory nucleus whose input to M1 pyramidal neurons had been characterized (Hooks *et al.*, 2015; Hooks *et al.*, 2013). Thalamic injections were determined in individual animals to be in PO and not anterior motor nuclei by the presence of axonal fluorescence in L1 and L5A. The absence of L5B fluorescence in these animals confirmed that our injections did not target motor thalamic nuclei, such as the anterior components of the ventroanterior-ventrolateral complex, which had previously been shown to

232 arborize in three distinct bands (L1, L5A, and L5B) instead of two (Hooks *et al.*, 2013). Targeting
233 recordings to tdTomato+ PV+ interneurons within the arborization of PO axons, we found that,
234 in contrast to S1 inputs, neurons in L5A received the strongest synaptic input (Fig. 6c).
235 However, input to PV+ cells in the top three layers of motor cortex (L2/3, L5A, and L5B) was
236 generally strong, without significant differences. Only synaptic input to L6 was weaker ($P<0.05$).
237 This input was not centered on the soma in the dendritic arbor, but instead was generally
238 targeted to the deep (white matter) side of proximal dendrites (Fig. 6d-f). This was the case for
239 all four layers measured (L2/3, L5A, L5B, and L6).
240 PO inputs to SOM+ interneurons were more difficult to characterize. We used the same
241 approach (Fig. 7) to quantify synaptic input. However, the pattern of input to SOM+ was noisy
242 and did not match any previous pattern observed for the other GABAergic cells (Fig 4-6) nor
243 pyramidal neurons previously recorded (Hooks *et al.*, 2013; Mao *et al.*, 2011). Instead, we found
244 that L5B was the most strongly excited layer (Fig. 7c), with significantly reduced input in L5A
245 ($p<0.001$). Comparisons to L2/3 and L6 were not significant and showed quite different patterns
246 across different cells, with some pairs favoring L2/3 or L6 and others favoring L5B. The
247 subcellular localization of input was also heterogeneous, with some SOM+ neurons in L5B and
248 L6 receiving input deep to the soma.
249 **Complementary patterns of input to specific interneuron types**
250 By comparing synaptic strength across layers and normalizing excitability to the
251 strongest input layer for multiple cell types, we were able to compare the pattern of input for the
252 same pathway to multiple cell types. We plotted the normalized input strength graph on the
253 same axes for S1 inputs or PO inputs to PV+ and SOM+ cells, as well as the same data
254 grouped by input to PV+ or SOM+ cells (Fig. 8a-d). This enabled a direct comparison of
255 S1 and PO input to PV+ and SOM+ neurons. Here, the same presynaptic afferents preferred
256 interneurons of different types in different layers. Considering the data organized by
257 postsynaptic target, cortical inputs from S1 to PV+ cells strongly preferred the uppermost (L2/3)
258 PV+ cells, while the functional targeting of PO inputs was biased toward deeper layers (L5A and
259 L5B; Fig. 8c). Input to SOM+ neurons showed a similarly complementary pattern, with input
260 from S1 axons most strongly exciting L5A, which is the layer least strongly excited by PO (Fig.
261 8d). Thus, the same type of interneuron is targeted in a different manner by the cortical and
262 thalamic inputs. For comparison, we plotted the input strength to excitatory neurons (Hooks,
263 2017). This pattern shows that S1 and PO generally target pyramidal neurons in the same layer
264 (Fig. 8e). We summarize all the synaptic strength experiments schematically in Fig. 8f, where
265 arrow thicknesses to specific cell types indicate cell-type specific connectivity.

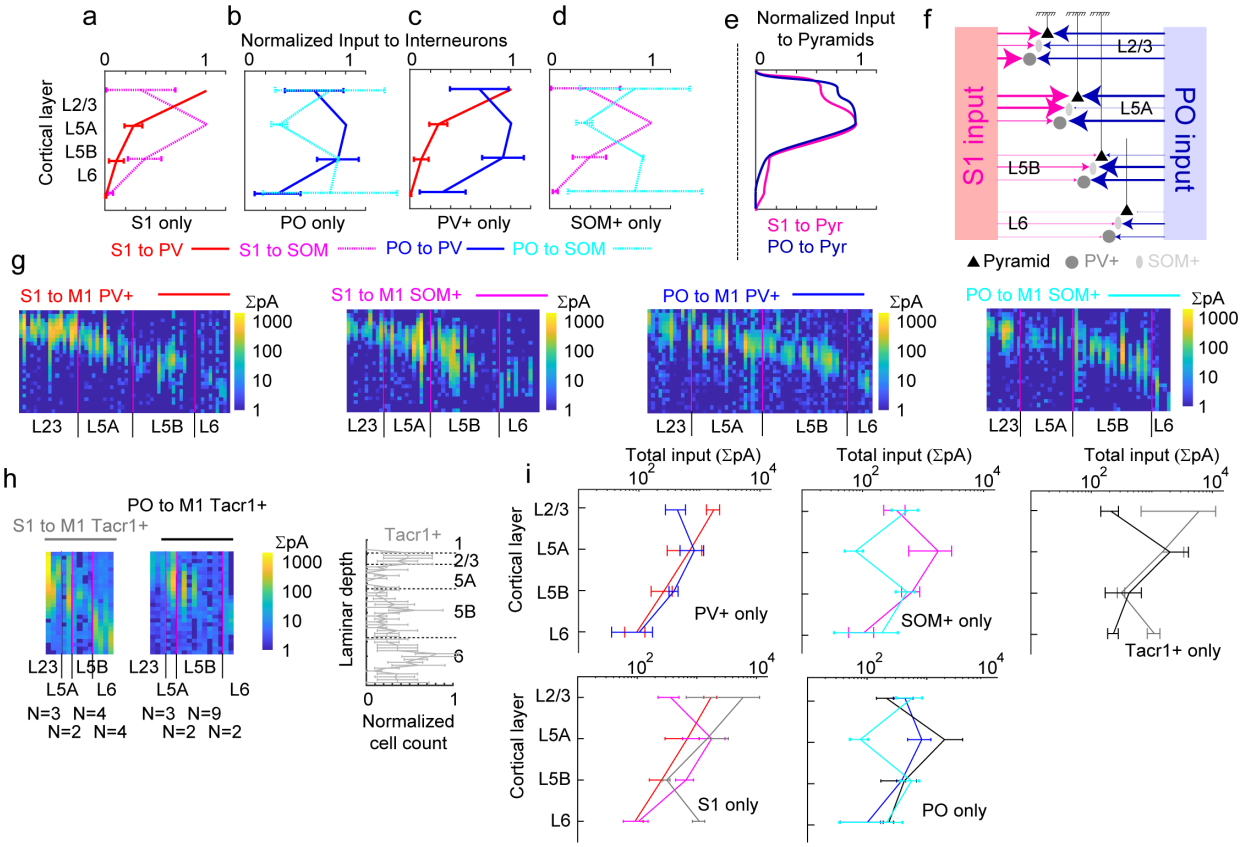

Figure 8 | Complementary patterns of input to specific interneuron types
(a-d) Summary graphs comparing the distribution of excitatory input to PV+ and SOM+ neurons. These plots compare normalized input from (a) S1 only or (b) PO only to PV+ and SOM+ neurons. (c-d) compare input to PV+ only (c) or SOM+ only interneurons. (e) The pattern of normalized input strength to pyramidal neurons (Pyr) from S1 and PO, after Mao et al (2011) and Hooks et al. (2013). (f) Cartoon summarizing input maps. (g) Absolute input strength for S1 and PO inputs, plotted as input vectors on a log scale. From left to right, S1 input to PV+ and SOM+ neurons and PO input to PV+ and SOM+ neurons. (h) Tacr1+ neurons (a subset of SOM+ neurons) presented in a similar fashion. Left, input maps from S1 and PO. For Tacr1+ neurons, N=3/2/4/4 for S1 input to L2/3, L5A, L5B, and L6; N=3/2/9/2 for PO input. Normalized laminar distribution of Tacr1+ somata (N=4 slices) measured at right. (i) Absolute input strength averaged by layer and plotted on a log scale for comparison between S1 and PO inputs (top row) to different interneuron types. Comparison of either S! or PO input to different interneuron types presented on the same axes (bottom row).

Because SOM+ neurons comprise a diverse range of neurons, including Martinotti and non-Martinotti subsets (Tremblay *et al.*, 2016), we were curious whether the input pattern to the SOM+ neurons labeled in our SOM-Cre x Ai14 strategy would be able to be replicated in a more targeted subset of cells (Huang et al., 2016; Tasic et al., 2018). We labeled the Tacr1+ subset of interneurons using a NK1R-CreER mouse crossed to a tdTomato reporter. Like SOM+ and PV+ crosses, this resulted in labeled neurons across the cortical thickness. We repeated our input mapping experiments in these mice and presented the data in a similar format (Fig. 8h). In contrast to all SOM+ and PV+ neurons, Tacr1+ cells responded well to S1 inputs across multiple layers. Of note, the strongest responses were in in L2/3 and L6, with weaker input to L5 (Fig. 8f-h). The input from PO also did not correspond to the SOM+ pattern, with strongly responding neurons in L5A and L5B.

278 Because our inputs to PV+ and SOM+ neurons were quantified as normalized input
279 strength, we wondered whether the absolute strength of input to PV+ and SOM+ differed across
280 pathways. We compared input across pathways and cell types by plotting the absolute input
281 strength for all cells on the same scale, as other investigators have done (Kinnischtzke et al.,
282 2014). This was done by summing the EPSC amplitudes across the points of the input map (as
283 in Fig. 3l). Cell vector plots were presented as before (Fig. 8g) using the same logarithmic scale
284 for all plots to improve presentation of more frequent recordings with weaker inputs. In general,
285 excitatory input from S1 and PO to either interneuron type (PV+ or SOM+, top and middle row)
286 was of similar magnitude. Averaging input by layer confirmed that monosynaptic input was of
287 comparable strength (Fig. 8i). The overall pattern is similar to our normalized data. The
288 distribution of S1 and PO input to PV+ is nearly overlapping, with the exception of input to L2/3
289 PV+ neurons. Input to SOM+ neurons is of similar strength from S1 and PO except for L5A,
290 where the absence of thalamic input is pronounced. Corticocortical input is similar or stronger to
291 SOM+ neurons than PV+ neurons at each laminar depth except L2/3. Thalamocortical input is
292 stronger to L5A PV+ neurons than to SOM+ cells. Outside of this layer, however, input strength
293 to SOM+ cells is equal to PV+ neurons.

294 **Direct comparison of synaptic and anatomical connectivity**

295 By performing comparable and anatomical experiments, we sought to make a
296 quantitative connection between input to PV+ and SOM+ neurons as measured by these distinct
297 methods. Differences in how the data are quantified presented challenges. First, because the
298 presynaptic neurons labeled by monosynaptic tracing might connect to a starter cell in any
299 cortical layer, we considered our anatomical tracing data to potentially present an averaged
300 view of connectivity to specific interneurons across all cortical layers. To make this data
301 comparable to our physiological data where target PV+ and SOM+ neurons were more explicitly
302 identified by laminar position, we sought to derive an average connection strength to PV+ or
303 SOM+ neurons by converting the layer-by-layer strength of synaptic connectivity (Fig. 9a, left)
304 into a weighted average strength (9a, at bottom) using the fractional distribution of PV+ and
305 SOM+ neurons (potential starter neurons) in each layer (Fig. 9a, middle) as weighting factors.
306 This not only determined the weighted average, but also by resampling the individual neurons
307 recorded in each category, a bootstrap mean (±SEM) could be determined to assess variability
308 of this estimate of physiological connectivity. The weighted averaged gave an idea of the
309 relative input strength to PV/SOM from cortical (0.7842) and thalamic (1.3724) input. This
310 suggested that monosynaptic thalamic input favored PV+ neurons, while corticocortical input

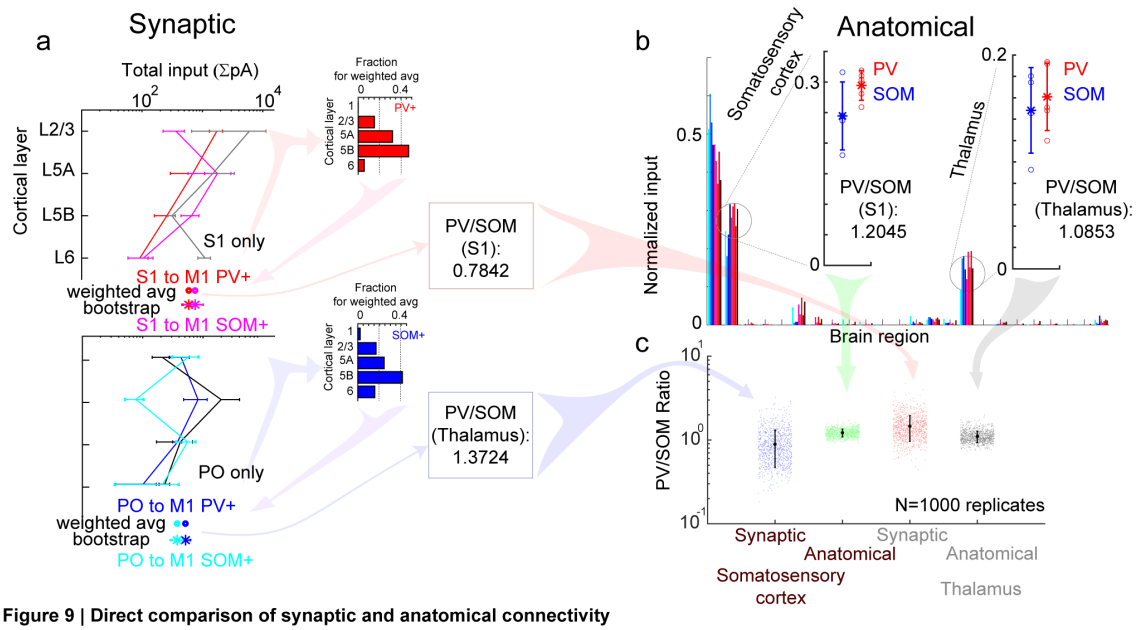

Figure 9 | Direct comparison of synaptic and anatomical connectivity
(a) Left, absolute synaptic input strength plotted for comparison between S1 inputs to PV+ and SOM+ neurons. Right, the distribution of interneurons per layer. The weighted average input strength is shown below the graph, either as a single point (weighted avg) or the mean and SEM from N=10000 replicate (bootstrap) analysis. The ratio of input to PV/SOM is shown for each plot. (b) Comparison of anatomical input to PV+ (N=5) and SOM+ (N=4) neurons in M1 from retrograde tracing (after Fig. 1). Insets show normalized fraction of input from each case. The ratio of input to PV/SOM is shown for each plot. (c) Comparison of PV/SOM input for synaptic inputs (from S1, red; from PO, green) and for anatomical tracing (in S1, blue; in thalamus, gray). The data was resampled for N=1000 replicates to compare.

might favor SOM+ neurons, likely because the strongest recipient layers for SOM+ (L5A and L5B) contained larger numbers of cells that the strongest PV+ recipient layer (L2/3). A ratio of PV/SOM input based on anatomical tracing (Fig. 9b) could also be determined. We quantified the mean fraction of presynaptic input in somatosensory cortex or thalamus. Using this as an anatomical connection strength, we then made a ratio between PV and SOM as done for synaptic input. Anatomical input from both somatosensory cortex (PV/SOM, 1.2045) and thalamus (1.0853) slightly favored PV+ neurons in M1. To explore the degree to which these ratios varied, we compared N=1000 bootstrap replicates of the synaptic and anatomical data, finding largely overlapping distributions (Fig. 9c).

Short term plasticity of long-range excitation to PV+ and SOM+ neurons

Our measurements of synaptic strength were based on monosynaptic input under recording conditions (TTX, CPP, 4-AP) which monitor synaptic responses to the first stimulus. These measurements might not reflect the relative contribution of the two interneuronal populations to a train of stimuli, which might be more physiological. Since PV+ and SOM+ neurons show differences in short term plasticity of local excitatory inputs (Beierlein et al., 2003), we were interested to test whether later synaptic inputs in a train might alter which interneuron population was more likely to carry feedforward inhibition.

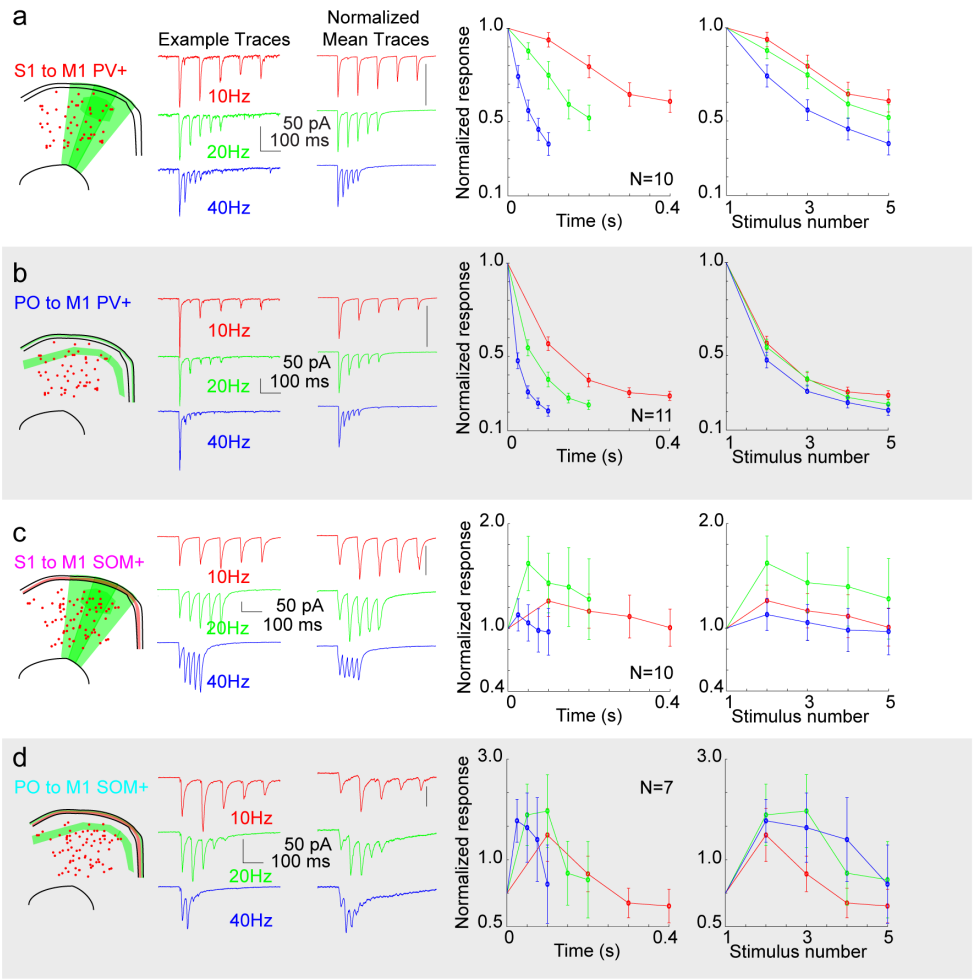

Figure 10 | Short-term plasticity at long range inputs to interneurons of mouse motor cortex
(a) Short term plasticity of S1 input to PV+ neurons. Left, example traces showing PV+ neuron response to S1 stimulation at 10 Hz (red), 20 Hz (green), and 40 Hz (blue) stimulation of Chronos-GFP+ S1 axons. Scale, 50 pA and 100 ms. Middle, average normalized traces for the same stimulus frequencies. Scale bar=1.0. Right, summary graphs showing normalized responses for 10 Hz, 20 Hz, and 40 Hz. Graphs are plotted based on time of the pulses (right) or the stimulus number (far right). (b) Short term plasticity of PO input to PV+ neurons, plotted as in (a). (c) Short term plasticity of S1 input to SOM+ neurons, plotted as in (a). (d) Short term plasticity of PO input to SOM+ neurons, plotted as in (a).

342 In contrast to these results in PV+ neurons, SOM+ cells showed some degree of
343 facilitation for both classes of input. S1 input was more facilitating at 20 Hz than 10 Hz.
344 Similarly, PO input was also more facilitating at 20 and 40 Hz. These experiments were
345 performed using the same viral vector and recording conditions for both mouse lines,
346 suggesting that the short-term plasticity observed differed between postsynaptic targets and
347 was not due exclusively to an artifact of measuring short term plasticity with optical methods
348 (Jackman et al., 2014). We do not know whether the same axon might have different release
349 properties depending on its cellular target (Beierlein *et al.*, 2003; Gabernet et al., 2005), or
350 whether different long-range axons from these areas preferentially innervate PV+ and SOM+
351 neurons.
352
353 **DISCUSSION**
354 Anatomical models for cortical connectivity propose that potential functional connectivity
355 is proportional to the overlap of axons and dendrites (Braitenberg and Schuz, 1998; Peters and
356 Feldman, 1976). However, a range of excitatory and inhibitory neurons exist in cortex (Tasic *et*
357 *al.*, 2018; Tremblay *et al.*, 2016), each with potentially cell type-specific rules for connectivity
358 and plasticity. Here we show that cortical and thalamic long-range inputs to M1 excite two types
359 of inhibitory interneurons in different and complementary ways. S1 inputs most strongly targeted
360 L2/3 PV+ neurons, but SOM+ neurons in middle layers (L5). Further, while S1 and PO both
361 targeted pyramidal neurons in L2/3 and L5A with similar connection strength, these pathways
362 targeted PV+ neurons in a different fashion. These results indicate that cortical and thalamic
363 afferents form highly specific connections in neocortex. Thus, the recruitment of feedforward
364 inhibition may not be simply a blanket of inhibition, but instead is divided into specific
365 feedforward circuits.
366 What is the functional relevance of specificity in feedforward connectivity? If incoming
367 afferents activate a selected subset of interneurons, then certain inputs will activate some
368 cortical networks while silencing others. For M1, this might mean activating the appropriate
369 response to incoming sensory stimuli, while inhibiting others. This would be of use, for example,
370 in selection or inhibition of one action over others. Pyramidal neurons in different cortical layers
371 project to different (but partially overlapping) long range targets, including corticocortical,
372 corticostriatal, corticothalamic, and pyramidal tract type projections (Harris and Shepherd, 2015;
373 Network, 2021). Thus, we hypothesize differences in laminar inhibition can shape the pattern of
374 M1 output to subsets of these targets. For example, S1 activation of L2/3 PV+ neurons might be
375 expected to most strongly silence output of L2/3 pyramids, resulting in reduced feedforward

excitation in both local inputs to L5 pyramidal neurons (Hooks *et al.*, 2011; Weiler *et al.*, 2008) as well as long-range corticocortical connections (Harris and Shepherd, 2015). This would vary during longer trains of stimuli as synapses to PV+ neurons depress. Notably, while both S1 and PO pathways excite L5B more weakly than other layers (Hooks *et al.*, 2013; Mao *et al.*, 2011), PO excited both PV+ and SOM+ interneurons in this layer, which might aid in terminating signals associated with inappropriate motor responses. Similarly, short-term plasticity differences in facilitation and depression may shape the timing and duration of inhibition, including low-pass or high-pass filtering of feedforward signals (Blackman et al., 2013). Thus, M1 computations performed on feedforward excitatory inputs from S1 and PO may be shaped by the relative amounts of facilitating and depressing inhibition recruited.

Specific circuits for feedforward inhibition

Motor cortex integrates a wide range of input from frontal cortical areas (Dum and Strick, 2002; Reep *et al.*, 1990; Rouiller *et al.*, 1993), primary and secondary sensory cortex (Chakraibarti and Alloway, 2006; Hoffer *et al.*, 2003; Kaneko *et al.*, 1994a; Smith and Alloway, 2013; Suter and Shepherd, 2015), retrosplenial cortex (Yamawaki et al., 2016), and different thalamic nuclei (Deschenes *et al.*, 1998; Kuramoto *et al.*, 2009; Ohno *et al.*, 2012; Strick and Sterling, 1974). These inputs activate M1 during voluntary and sensory guided movement, with each targeting excitatory neurons in M1 in a layer-specific manner (Hooks *et al.*, 2013). Different M1 neurons can represent either sensory input or motor behavior such as whisking, licking, or lever pressing (Harrison and Murphy, 2014; Huber *et al.*, 2012; Masamizu et al., 2014; Tanaka et al., 2018), suggesting that individual neurons are parts of different networks, receiving input of different strength from cortical inputs. Here we tested whether this pattern is the same for functional synaptic input to interneurons, finding that the laminar pattern of excitation varies with the postsynaptic cell type targeted.

Each excitatory pathway evokes feedforward inhibition to some degree (Isaacson and Scanziani, 2011). This disynaptic inhibition might serve to terminate continuing excitation from the same inputs. Once recruited, local circuit interneurons connect to large numbers of nearby pyramidal neurons (Bock et al., 2011; Fino and Yuste, 2011; Packer and Yuste, 2011). If synaptic weights are strong, this might provide an effective suppression of cortical activity (Fino et al., 2013), though the effectiveness of these connections could be reweighted by activity-dependent (Xue et al., 2014) or experience-dependent (Chen et al., 2015) plasticity mechanisms. Thus, it is of interest to understand whether the recruitment of feedforward inhibition proceeds through distinct interneurons (of either the same or different type) for inputs recruiting motor cortex. Our data indicates that there is space for selectivity in inhibitory circuitry.

410 Some specific examples of differences stand out in our quantitative maps. Our data
411 suggests that the incoming sensory information from S1 excites PV+ neurons in L2/3 but SOM+
412 neurons in L5. Since these same afferents from S1 also strongly target pyramidal neurons in
413 L2/3 and L5A (Mao *et al.*, 2011), it suggests that, in part, the feedforward inhibition recruited to
414 L2/3 pyramids and L5A pyramids can proceed through different neural populations, as cortical
415 interneurons generally, though not exclusively, inhibit pyramidal neurons in the same layer
416 (Katzel *et al.*, 2011). Since SOM+ neurons may also inhibit PV+ cells, helping to disinhibit cortex
417 (Pfeffer et al., 2013), it is possible that S1 input can have differential inputs on the excitability of
418 L2/3 and L5A pyramids, despite similarity in monosynaptic excitation to these targets. This
419 suggests that differences in cell types play a role in determining the efficacy of feedforward input
420 and the rules of long-term plasticity in these two target layers. The pattern of thalamic input to
421 PV+ interneurons also differed from S1 input. This suggests that where cortical and thalamic
422 afferents target the same excitatory network, to the extent S1 and PO target partially non-
423 overlapping PV+ populations, feedforward inhibition recruited by one pathway would not be as
424 strongly depressed by the recruitment of PV+ inhibition by the other pathway arriving at a similar
425 time.
426 Of note, PO provided fairly strong input to both PV+ and SOM+ neurons in L5B (Fig. 8g-
427 h). This feedforward inhibition would potentially inhibit L5B pyramidal neurons, which are only
428 weakly excited by S1 and PO L5A (Hooks *et al.*, 2013; Mao *et al.*, 2011). We infer the net effect
429 would be to reduce activity in L5B pyramidal neurons. It is unknown if there is specific targeting
430 to certain pyramidal neuron subtypes. L5B contains two main classes of output neurons,
431 IntraTelecephalic type cells projecting to both cortex and striatum, as well as Pyramidal Tract
432 type cells which mainly target thalamus, brainstem, and spinal cord (Hooks et al., 2018;
433 Shepherd, 2013). Thus, a range of cortical output channels might be suppressed. The function
434 of inhibiting neurons outside the normal targets of excitation of these pathways is unknown, but
435 by reducing overall activity of M1 output neurons might serve to set a higher threshold of
436 activation in the context of incoming sensory information. By reducing background activation,
437 this would increase the signal to noise ratio of outgoing motor signals.
438 **Organization of long-range input to SOM+ interneurons differs across cortical areas**
439 It had previously been shown that SOM+ neurons in L4 of sensory areas generally
440 received weaker input than neighboring pyramidal neurons and PV+ neurons (Bruno and
441 Simons, 2002; Cruikshank *et al.*, 2007; Cruikshank *et al.*, 2010). This thalamocortical preference
442 for PV+ over SOM+ neurons in somatosensory cortex extends to L2/3 (Naskar et al., 2021).
443 Thalamic input to SOM+ does exist in sensory areas, though it may be developmentally

444 downregulated at ages younger than those studied here (Marques-Smith et al., 2016;
445 Tuncdemir et al., 2016). Thus, we were surprised to find many layers in M1 where SOM+ cells
446 received comparable inputs to PV+ cells (Fig. 8) as measured by monosynaptic input mapping
447 (Porter et al., 2001). Comparisons are challenging due to limitations of normalizing input
448 strength across different injections in different animals (Petreanu *et al.*, 2009), but the mean
449 thalamic input strength to SOM+ interneurons was marginally higher than that to PV+ neurons
450 except for L5A (Fig. 8h middle right). However, there is considerable variability between
451 individual cells (Fig. 8g). Similarly, corticocortical input from S1 was higher to SOM+ neurons in
452 L5A and L5B (Fig. 8h top right). This collectively suggests that there is no uniform rule that
453 thalamic input will be selective for PV+ neurons across all cortical areas and layers.
454 In addition to monosynaptic input strength, it is also worth considering that input from S1
455 and PO will not occur in isolation but as part of trains of action potentials, especially should
456 thalamus fire in burst mode (Sherman, 2001; Steriade et al., 1993). In the case of PO, short
457 term depression of input to PV+ neurons is the strongest short term plasticity we observed (Fig.
458 10). In contrast, these inputs were facilitating to SOM+ neurons. This suggests that as rapidly
459 as the second or third pulse in a train, the recruitment of feedforward inhibition could shift from
460 PV+ to SOM+ neurons (Tan et al., 2008). The difference in short term facilitation and
461 depression to SOM+ and PV+ neurons respectively is not as large for S1 afferents as for PO
462 inputs, though the general pattern is the same. This effect is qualified by differences in the
463 intrinsic excitability of the particular cells involved, as well as their own depression onto
464 pyramidal neuron targets. Inhibition from SOM+ neurons is hypothesized to be facilitating, in
465 contrast to the depression observed in fast spiking neurons (Beierlein *et al.*, 2003). If this is the
466 case in M1, then this would serve to further shift the balance of disynaptic feedforward inhibition
467 from PV+ to SOM+ neurons, giving SOM+ neurons the potential to play a role in regulating
468 excitability and plasticity (Chen *et al.*, 2015).

469 **Comparison of anatomical and functional methods for mapping microcircuitry**

470 The emergence of techniques for recording, imaging, and reconstructing the whole brain
471 present a great deal of data to deepen our understanding of how neocortical areas are
472 connected and function at large scales. Imaging projections from defined neurons (Jeong et al.,
473 2016; Oh *et al.*, 2014; Zingg *et al.*, 2014) to label long-range targets or retrograde viral methods
474 to label presynaptic inputs (Luo et al., 2018; Wickersham et al., 2007a) offers hope for efficiently
475 identifying long-range connections in whole brains when images are aligned to standardized
476 coordinate systems (Eastwood et al., 2019; Hooks *et al.*, 2018; Kuan *et al.*, 2015). Thus,
477 monosynaptic tracing with rabies virus has substantial appeal. Ideally, a comparison across

478 large scale recording methods (such as probes with numerous channels or imaging calcium
479 responses in large neuron populations), synaptic connectivity, and anatomical projections would
480 help clarify how neural connectivity contributes to brain function.
481 Here we directly compared synaptic input and retrograde anatomical tracing of
482 presynaptic input to M1 interneurons. Based on prior work, we hypothesized that
483 thalamocortical input would favor PV+ interneurons. In S1, thalamic inputs to fast spiking
484 (presumed PV+) neurons were more likely to be connected (Bruno and Simons, 2002) and were
485 vastly stronger by EPSC amplitude, as much as 10-20x in L4 and L5/6 (Fig. 6, (Cruikshank *et*
486 *al.*, 2010)) as well as later 2/3 (Fig. 2, (Naskar *et al.*, 2021)). In M1 by contrast, both synaptic
487 connectivity mapping experiments and retrograde viral tracing data showed strong
488 thalamocortical connections to PV+ and SOM+ neurons in M1 (Figs. 1 and 6-9). Indeed, input to
489 PV+ neurons was only ~10-30% stronger than that to SOM+ neurons (Fig. 9). This difference
490 was not significant in the anatomy data, though non-significant trends (Fig. 1) were present in
491 three thalamic nuclei not assessed functionally (VM, PC, and PF). Thus, both measures of
492 anatomical and functional connectivity were consistent in demonstrating distinct thalamocortical
493 connectivity rules for primary motor cortex compared to sensory cortex. Similarly, our measures
494 of corticocortical input to SOM+ neurons were comparable between anatomical and functional
495 methods (Fig. 9), though the functional method showed a slight preference for SOM+ neurons
496 (because of stronger input to the more numerous interneuron population in L5A and L5B), while
497 the anatomical method showed a nonsignificant trend for larger S1 input to PV+ neurons (Fig.
498 1). This is in contrast to corticocortical input in S1, where long range input to PV+ neurons was
499 stronger in L2/3 for multiple pathways (Naskar *et al.*, 2021).
500 However, there are some limitations to the comparison. With anatomical methods, it was
501 not possible to label SOM+ or PV+ interneurons in specific layers and show differences in
502 connectivity as was the case in functional mapping experiments. Furthermore, quantifying
503 differences in synaptic strength is not precisely the same as labeled presynaptic neurons.
504 Although we hypothesize that stronger synaptic connections would result in more points of
505 contact between corticocortical or thalamocortical axons and rabies-infected starter cells, there
506 are not control experiments to show that increased synaptic strength results in an increase in
507 labeled presynaptic neurons. Furthermore, while we can quantify synaptic strength to PV+ or
508 SOM+ neurons from S1 or PO inputs in a given layer, it is not certain that deriving a single value
509 for connection strength for the whole population is the strongest means to make such a
510 comparison.

How reliable is retrograde labeling for anatomically assessing connectivity? The data presented here suggest anatomical and functional methods can predict similar connectivity. First, the retrograde tracing data provides strong support for retrograde tracing as an effective measure of area-to-area connectivity. Tracing from starter cells in each cortical area specifically labeled cortical areas and a pattern of thalamic nuclei unique to that cortical area and reproducibly across replicates (Fig. 2b-e). For example, M2 gets input from limbic areas while M1 and S1 do not. Furthermore, even small brain areas, such as individual thalamic nuclei, have distinct patterns of label for each of the three cortical areas studies. However, because the specific thalamic labeling was almost identical for input to PV+ and SOM+ interneurons for the regions that we studied, evidence that retrograde tracing varies strongly with postsynaptic target would be better to test in cell types with vastly different connectivity, especially where afferents avoid innervating one cell type while connecting strongly to another intermingled type.

Subcellular organization of input to interneurons

Our circuit mapping approach gives some insight into the subcellular localization of synaptic input in the dendritic arbor of postsynaptic neurons. This insight is constrained by methodological limitations of patch clamp which limit our ability to study distal dendrites. Interneurons, however, are generally more electronically compact than pyramidal neurons. There is some organization of the input around the PV+ and SOM+ soma, suggesting some mechanisms for afferent targeting exist and may differ between interneuron subtypes. S1 input to PV+ neurons is evenly distributed perisomatically, while these same afferents tend to target dendrites ~50-150 μm below the soma of SOM+ cells. Similarly, PO input to PV+ cells is also shifted deep to the soma center by ~50-150 μm. This offset is interesting in contrast to thalamic inputs to pyramidal neurons (Petreanu *et al.*, 2009). In these cells, PO input targets the apical dendrites, and especially the L1 arbors of L3 pyramidal neurons but is soma-centered (and quite strong) for L5A pyramidal neurons. This is consistent with each cell type directing input from a defined presynaptic pathway to some extent within its arbor.

Different SOM+ subtypes have different connectivity

One difficulty in making a general statement about SOM+ connectivity in M1 was the variability within this dataset, especially for thalamic inputs (Fig. 7). In our assessment of monosynaptic input strength and short-term plasticity, PV+ neurons behaved in a much more homogeneous manner. These are the largest GABAergic neuron population defined by a single immunohistochemical marker (~40%), consisting of mostly perisomatic-targeting basket cells, though this group also includes axon-targeting chandelier cells (Tremblay *et al.*, 2016). In contrast, SOM+ neurons (~30%) include distal dendrite targeting Martinotti-type neurons,

545 evident in the L1 axonal fluorescence in Fig 3f, as well as multiple non-Martinotti types. Thus,
546 SOM+ neurons include at least two (and likely more) molecular subtypes (Ma et al., 2006; Naka
547 et al., 2019; Tasic *et al.*, 2018; Zeisel et al., 2015), which might account for the variability in the
548 data. One subset of SOM+ interneurons expresses Tacr1, as well as NPY and nNOS (Kubota et
549 al., 2011), though these have differences in nNOS expression level (Dittrich et al., 2012).
550 Tacr1+ cells, like both PV+ and SOM+ neurons are present across cortical layers 2-6. This
551 made comparison of input strength possible. This was not the case for VIP+ neurons, which are
552 much more numerous in only upper layers (~60% in L2/3 (Pronneke et al., 2015)), as well as
553 other non-VIP expressing 5HT3aR+ interneurons which are similarly biased to L1 and L2/3 (Lee
554 *et al.*, 2010).
555 When synaptic strength was mapped, this presented a pattern of input strength quite in
556 contrast to that of the SOM-Cre x Ai14 mice (Fig. 8h-i). In particular, S1 input had been
557 distributed across L2/3, L5A, and L5B to SOM+ neurons, but most strongly to L5A. In contrast,
558 this subset had a quite distinct pattern, with substantial L2/3 and L6 input. PO input was noisy
559 to SOM+ neurons in general. This emphasized the likelihood that each molecular subtype of
560 interneuron had distinct mechanisms to govern synaptic strength.

561 **Conclusion**

562 Overall, these results point towards circuit mechanisms by which different pathways of
563 incoming excitation may excite specific subcircuits, including specific networks for inhibition in
564 primary motor cortex. Having some means by which recruitment of feedforward inhibition from
565 each pathway does not generally silence all M1 circuits is perhaps necessary for control of
566 movement when M1 is receiving competing inputs from different brain regions.
567

568 **MATERIALS AND METHODS**

569 **Stereotactic injections.**

570 Animal protocols were approved by Institutional Animal Care and Use Committee at University
571 of Pittsburgh (Protocol #20118160) and followed the recommendations in the Guide for the Care
572 and Use of Laboratory Animals of the National Institutes of Health. Mice of either sex were
573 used. Experimental procedures were similar to previous studies (Hooks *et al.*, 2013). Cre driver
574 mouse lines (PV-Cre, SOM-Cre, and NK1R-CreER) were used in conjunction with the lsl-
575 tdTomato reporter line, Ai14, to label specific interneuron populations (see Table 2). Tacr1
576 experiments using NK1R-CreER, required tamoxifen injections to drive recombination. Animals
577 were anesthetized using isoflurane and placed in a custom stereotactic apparatus. Juvenile
578 mice at postnatal (P) day P12-P22 were injected with AAV expressing excitatory opsins. AAVs

579 included CAG-ChR2-mVenus and hSyn-Chronos-GFP. AAV-CaMKIIa-hChR2(H134R)-EYFP
580 was used in Tacr1 mapping experiments (see Table 3 for details and serotypes). Injections were
581 made with glass pipettes (Drummond) using a custom-made positive displacement system
582 (Narashige). Stereotactic coordinates are listed in Table 1. A pair of injections (50-100 nL; 500
583 and 800 μm depth from pia) was made in the cortex. One location (50-100 nL) was injected into
584 thalamic targets.
585 **Monosynaptic viral tracing.** We used AAV injections to express DIO-TVA-EGFP-B19G in
586 potential starter cells in cerebral cortex of PV-Cre and SOM-Cre driver mouse lines (Atasoy et
587 al., 2008; Wickersham *et al.*, 2007b). After two weeks of expression time, we injected EnvA
588 pseudotyped rabies (CVS-N2c$^{\Delta G}$ strain) into cortex and allowed 8-9 days for transport and
589 expression (Reardon *et al.*, 2016). Following transcardial perfusion, whole brains were
590 sectioned, immunoamplified for EGFP and TdTomato, and stained with NeuroTrace Blue
591 (ThermoFisher) as a structural marker. The brain was imaged and reconstructed using
592 NeuroInfo software (MBF Bioscience) as previously described (Eastwood *et al.*, 2019; Hooks *et*
593 *al.*, 2018). Original images are posted at: http://gerfenc.biolucida.net/link?l=JI1tV7 (Biolucida
594 Cloud Viewer, free download) and
595 http://gerfenc.biolucida.net/images/?page=images&selectionType=collection&selectionId=32
596 (web-based). Images were aligned to the Allen CCF V3.0 (Kuan *et al.*, 2015; Oh *et al.*, 2014)
597 using NeuroInfo software (MBF Bioscience). Somata were detected by NeuroInfo using an
598 artificial neural network. Their coordinates in the Allen CCF used to quantify in which structure
599 the neuron was detected using custom Matlab software. Presynaptic labeled (tdTomato+)
600 neurons in each structure were quantified as a fraction of total labeled neurons in that brain to
601 normalized for differences between mice and injections. For comparisons between starter cell
602 types (PV+ or Cre+) or injection sites (M2, fM1, vS1), t-tests were performed. To reduce the
603 number of comparisons to a manageable size, brain regions were only included in the analysis if
604 the fraction of presynaptic neurons labeled exceeded a threshold value: 2% for 24 large brain
605 areas (Fig. 1o and Fig. 2bd) or 0.5% for 33 smaller thalamic nuclei (Fig. 1p and 2c and 2e-h).
606 The two-stage procedure of Benjamini, Krieger, & Yekutieli (Benjamini *et al.*, 2009) was used to
607 control for the false discovery rate (FDR). Black * (with p-values noted) mark significant
608 differences between presynaptic labeling. Gray * used for comparisons not significant after
609 correcting for FDR.
610 **Electrophysiology and photostimulation.** Brain slices were prepared >14 days after viral
611 infection, in young adult mice (~P30-P60). Mice were anesthetized with isoflurane and the brain
612 was rapidly removed and placed in cooled choline-based cutting solution (in mM: 110 choline

613 chloride, 3.1 sodium pyruvate, 11.6 sodium ascorbate, 25 $NaHCO_3$, 25 D-glucose, 7 $MgCl_2$, 2.5
614 KCl, 1.25 NaH_2PO_4, 0.5 $CaCl_2$). Off-coronal sections (300 µm) of M1 were cut using a vibratome
615 (VT1200S, Leica). Additional sections were cut to confirm injection location. Slices were
616 incubated at 37 ºC in oxygenated ACSF (in mM: 127 NaCl, 25 $NaHCO_3$, 25 D-glucose, 2.5 KCl,
617 2 $CaCl_2$, 1 $MgCl_2$, 1.25 NaH_2PO_4,) for >30 min and maintained at room temperature (22 ºC)
618 thereafter.
619 Whole cell recordings were performed at 22 ºC in oxygenated ACSF with borosilicate
620 pipettes (3-6 MΩ; Warner Instruments) containing potassium gluconate-based internal solution
621 (in mM: 128 potassium gluconate, 4 $MgCl_2$, 10 HEPES, 1 EGTA, 4 Na_2ATP, 0.4 Na_2GTP, 10
622 sodium phosphocreatine, 3 sodium L-ascorbate; pH 7.27; 287 mOsm). These recordings
623 targeted neurons in whisker M1 for whiskers (vM1, coordinates in Table 1). In some
624 experiments, biocytin was added to the intracellular solution (3 mg/mL biocytin or neurobiotin).
625 For subcellular ChR2-Assisted Circuit Mapping (sCRACM) experiments (Petreanu *et al.*,
626 2009), TTX (1 µM, Tocris), 4-AP (0.1-0.3 mM, Sigma) and CPP (5 µM, Tocris) were added to
627 the bath. Dose-response of 4-AP concentration was confirmed in a subset of experiments
628 comparing EPSC amplitude while 4-AP was added. Under these conditions, laser pulses (1 ms)
629 depolarized ChR2-expressing axons in the vicinity of the laser beam and triggered the local
630 release of glutamate. Measurements of postsynaptic currents then revealed the presence of
631 functional synapses between ChR2-expressing axons and the recorded neuron near the
632 photostimulus. Blocking action potentials prevented polysynaptic contributions.
633 Data were acquired at 10 kHz using an Axopatch 700B (Molecular Devices, Sunnyvale,
634 CA) and Ephus software (www.ephus.org) (Suter et al., 2010) on a custom-built laser scanning
635 photostimulation microscope (Shepherd et al., 2003). During sCRACM mapping, neurons were
636 held at -70 mV. A blue laser (473 nm, CrystaLaser) was controlled via scan mirrors (Cambridge
637 Technology). Light pulses were controlled with a shutter (4 ms open time) in series with an
638 acousto-optic modulator (1 ms pulse, Quanta-Tech) to deliver ~0.5-2 mW at the specimen plane
639 through a low power objective (4x, 0.16 NA, UPlanApo; Olympus). Laser power was constant
640 during a given day. Sweep consisted of 100 ms baseline and 300 ms following onset of the
641 stimulus. The map grid (12x26 sites at 50 µm spacing) was centered horizontally over the soma
642 of the recorded neuron, aligned at its upper edge to the pia, and covered the entire interneuron
643 dendritic arbor. Maps were repeated 2-4 times and averaged across trials. Stimuli for short term
644 plasticity were delivered using 1ms flashes of a 470 nm LED (Cairn). Sweeps were interleaved
645 and repeated 4-6 times per stimulus frequency.

Data analysis. Data analysis was performed with custom routines written in Matlab. Electrophysiology data were low pass filtered (1 kHz). EPSCs were detected with a threshold of >6x standard deviation from baseline). Mean EPSC amplitude for input maps was averaged over 75 ms post-stimulus (reported in pA). For comparison between cells in the same slice, total input was computed by summing supratheshold pixels. Paired comparisons across cells use the nonparametric Wilcoxon signed-rank test. Mean ratio of excitation were calculated as geometric means, with the strongest input layer shown as 1.0. In these comparisons, the bar graph was overlaid with a line showing the bootstrap mean and SD (10000 replicates) resampling the paired data. To compare the axonal profile of S1 and PO axons (Fig. 1), we quantified the fluorescence as before (Hooks *et al.*, 2013) by determining the mean fluorescence of pixels at a given laminar depth (binned in 50 bins across cortex from pia to white matter). N are reported in figures for number of cells. Number of mice used are: N=15 (S1 to M1 PV+), N=12 (PO to M1 PV+), N=10 (S1 to M1 SOM+), N=10 (PO to M1 SOM+), N=4 (S1 to M1 Tacr1+), and N=4 (PO to M1 Tacr1+).

662 **TABLES**

663 **Table 1. Injection coordinates**

664 Anterior/posterior (A-P) axis reported relative to bregma (positive values anterior to bregma).
665 Medial/lateral (M-L) axis reported relative to the midline. Dorsal/ventral (D-V) axis, depth from
666 pia. Injections were made at both depths in cortex. Distances in mm.

Target	A-P	M-L	D-V
Primary whisker motor cortex (vM1)	+1.1	0.9	0.5/0.8
Posterior thalamus (PO)	-1.2	1.3	2.75
Primary whisker somatosensory cortex (vS1)	-0.6	3.0	0.5/0.8
For rabies tracing			
Secondary motor cortex (M2)	+2.6	1.0	0.5/0.8
Forelimb motor cortex (fM1)	+0.6	1.5	0.5/0.8
Primary whisker somatosensory cortex (vS1)	-0.6	3.0	0.5/0.8

667

668 **Table 2. Mouse lines**

Mouse Lines	Line #	Reference
PV-Cre	JAX 017320	(Hippenmeyer et al., 2005)
SOM-Cre	JAX 017320	(Taniguchi et al., 2011)
Ai14	JAX 007914	(Madisen *et al.*, 2010)
NK1R-CreER	JAX 035046	(Huang *et al.*, 2016)

669

670 **Table 3. Viral reagents**

Virus	Serotype	Addgene #
CAG-ChR2-mVenus	AAV1, AAV9, and AAV10	20071
hSyn-Chronos-GFP	AAV1, AAV5, and AAV9	59170
CaMKIIa-hChR2(H134R)-EYFP	AAV9	26969
DIO-TVA-EGFP-B19G	AAV1	52473
N2c-ΔG-EnvA-tdTomato	CVS-N2c rabies	n/a

671

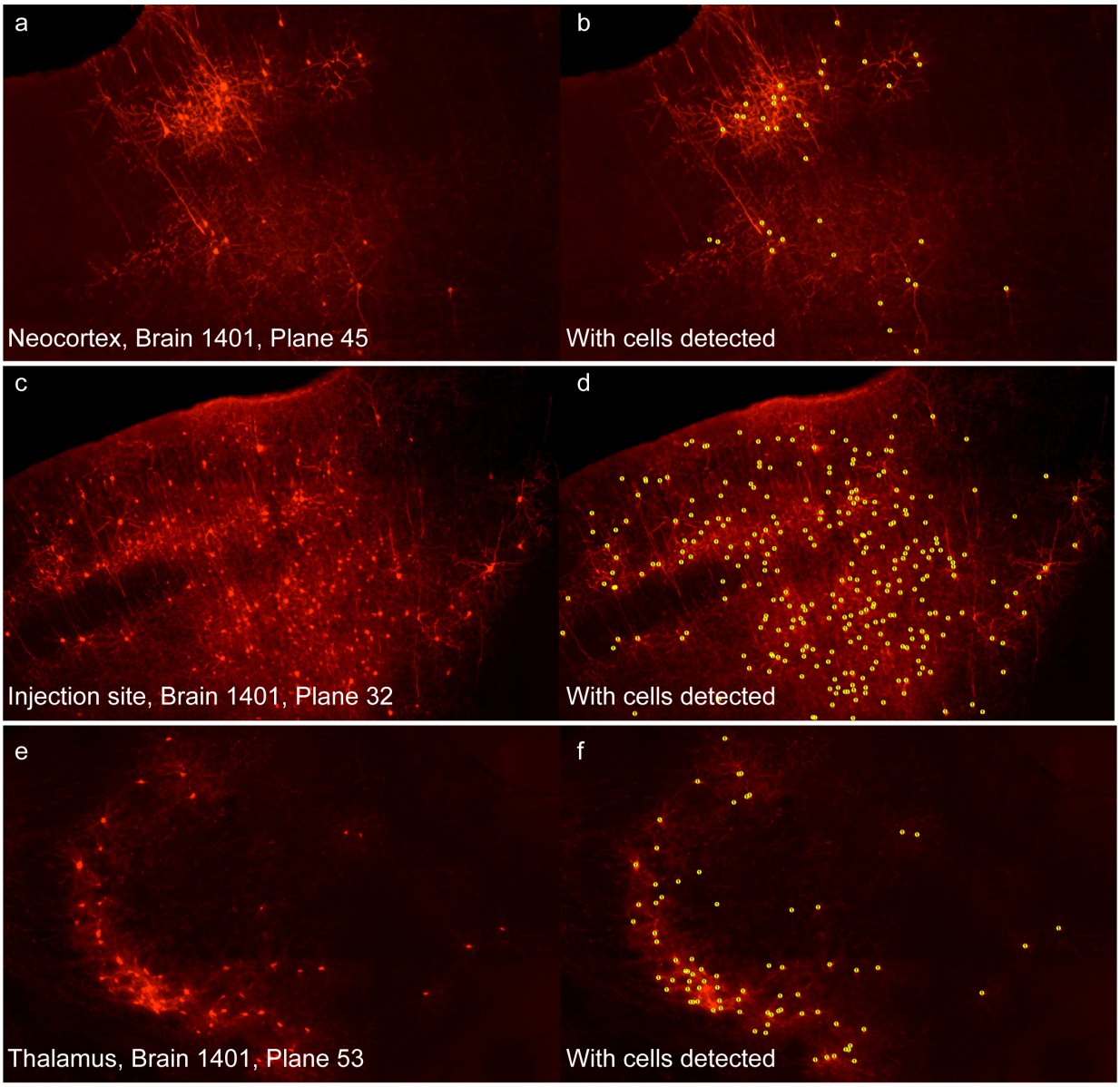

Supplemental Figure 1 | Cell detection in cortex and thalamus
(a-b) Low density cortical labeling from monosynaptic rabies tracing in M1 of a SOM-Cre mouse. (a) Cells in somatosensory neocortex posterior to the injection site. (b) The same plane with cells detected. (c-d) High density cortical labeling near the injection site in M1 of a SOM-Cre mouse. (e-f) Thalamic labeling in a SOM-Cre mouse.

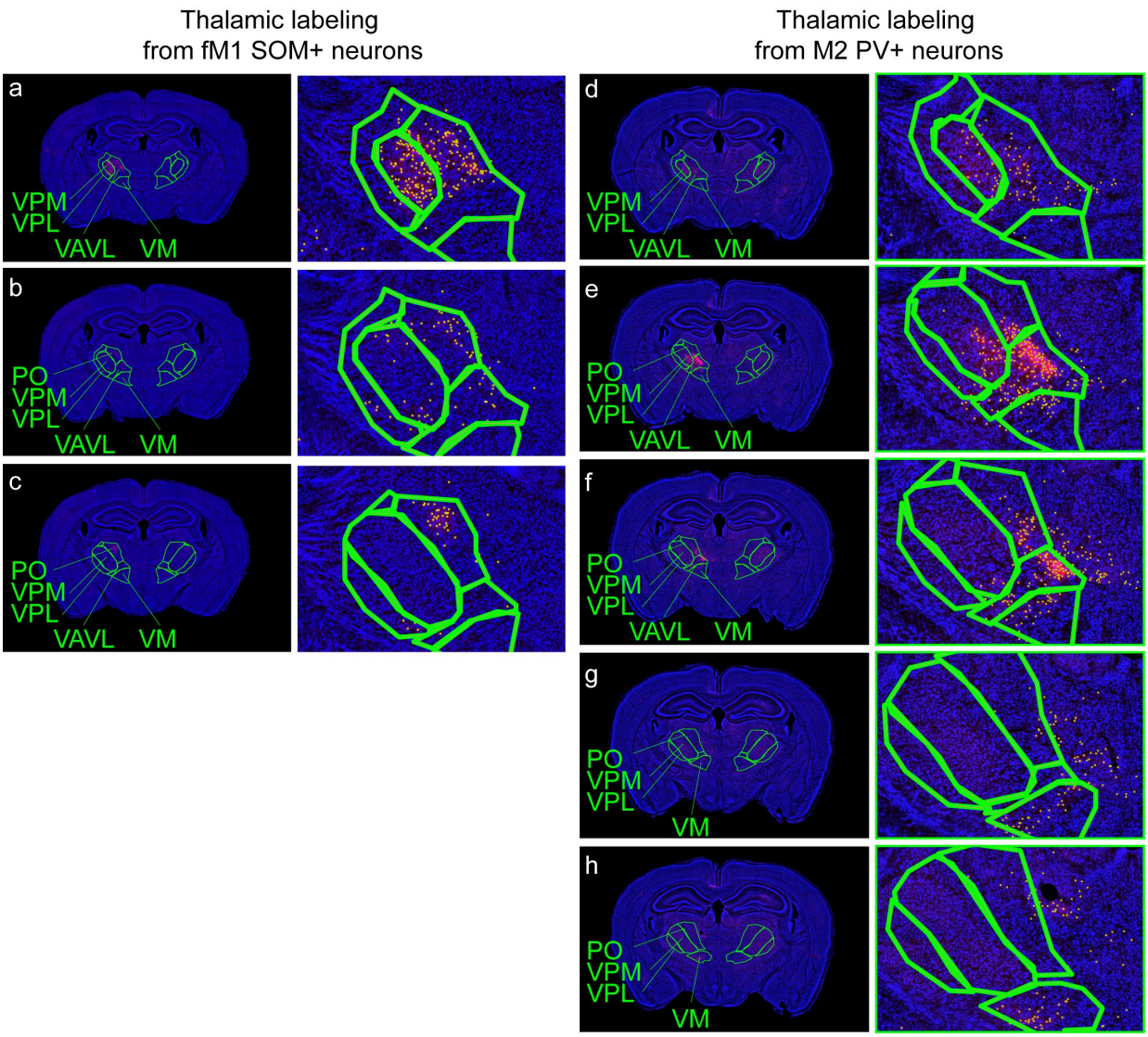

Supplemental Figure 2 | Thalamic labeling in from SOM+ and PV+ neurons
(a-c) Retrograde labeling from fM1 SOM+ neurons. Left panel, structural stain (Neurotrace Blue) and retrogradely labeled neurons (tdTomato, red). Thalamic nuclear boundaries based on registration to CCF V3.0 atlas. Nuclei as indicated. Right panel, higher magnification version. Detected cells labeled by yellow circles. Planes shown are separated by ~0.16 mm proceeding from anterior (top, a) to posterior (bottom, c).
(d-h) Retrograde labeling from M2 PV+ neurons. Left panel, structural stain (Neurotrace Blue) and retrogradely labeled neurons (tdTomato, red). Thalamic nuclear boundaries based on registration to CCF V3.0 atlas. Nuclei as indicated. Right panel, higher magnification version. Detected cells labeled by yellow circles. Planes shown are separated by ~0.16 mm proceeding from anterior (top, d) to posterior (bottom, h).
PO, posterior thalamic nuc.; VAVL, ventoanterior/ventrolateral thalamic nuc.; VM, ventromedial thalamic nuc.; VPL, ventroposteriolateral thalamic nuc.; VPM, ventroposteriomedial thalamic nuc.

673

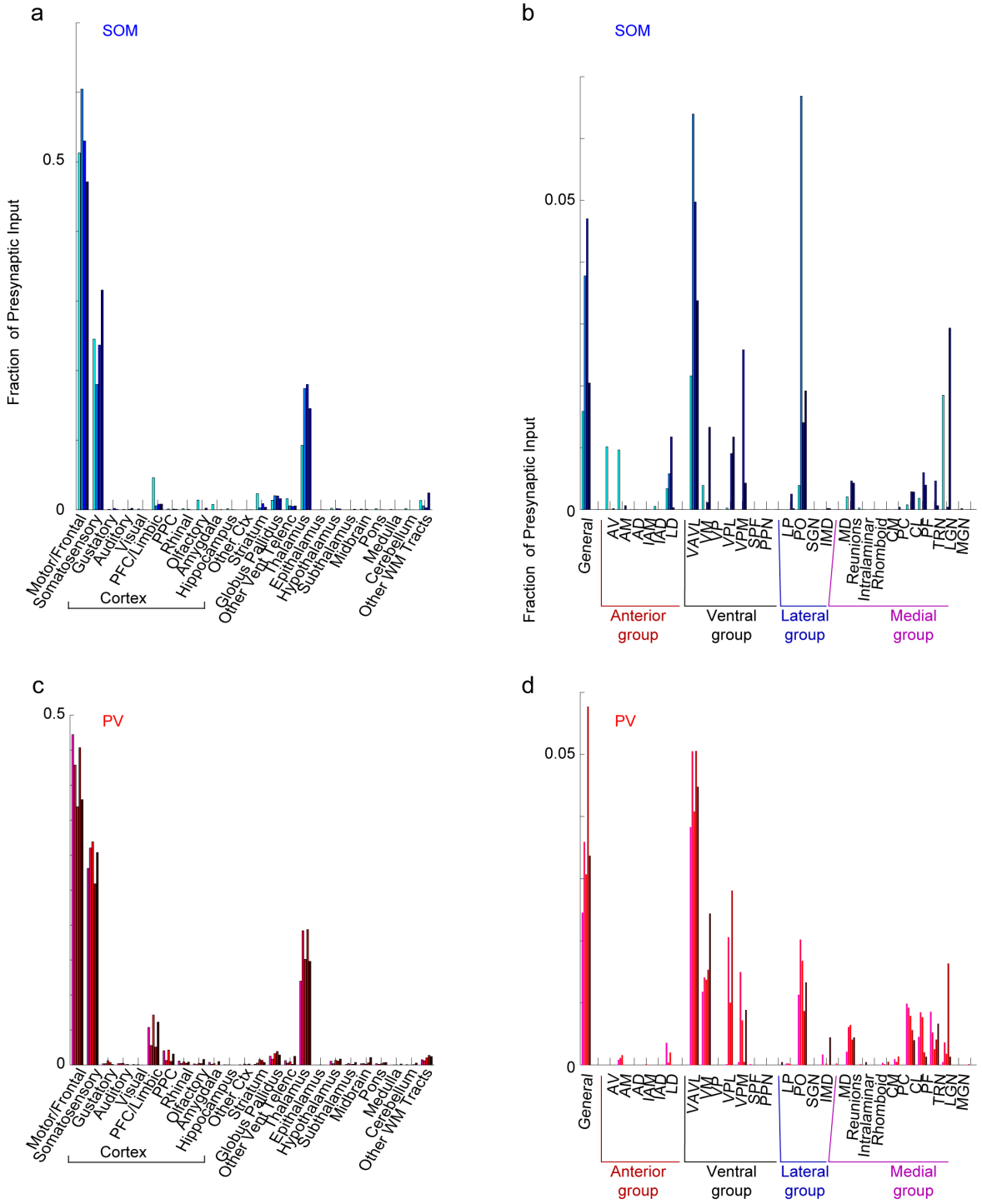

Supplemental Figure 3 | Consistency of monosynaptic retrograde tracing
(a-b) Quantification of presynaptic neuron location in the whole brain (a) and thalamus (b) plotted as bar graphs to emphasize differences between individual retrograde tracing cases. For SOM-Cre (N=4, blue) mice, the fraction of the total presynaptic neuron population (±SEM) plotted for all M1 injections. Bars represent individual cases. (c-d) Quantification of presynaptic neuron location in the whole brain (a) and thalamus (b) for PV-Cre (N=5, rec) mice, plotted as above.

674

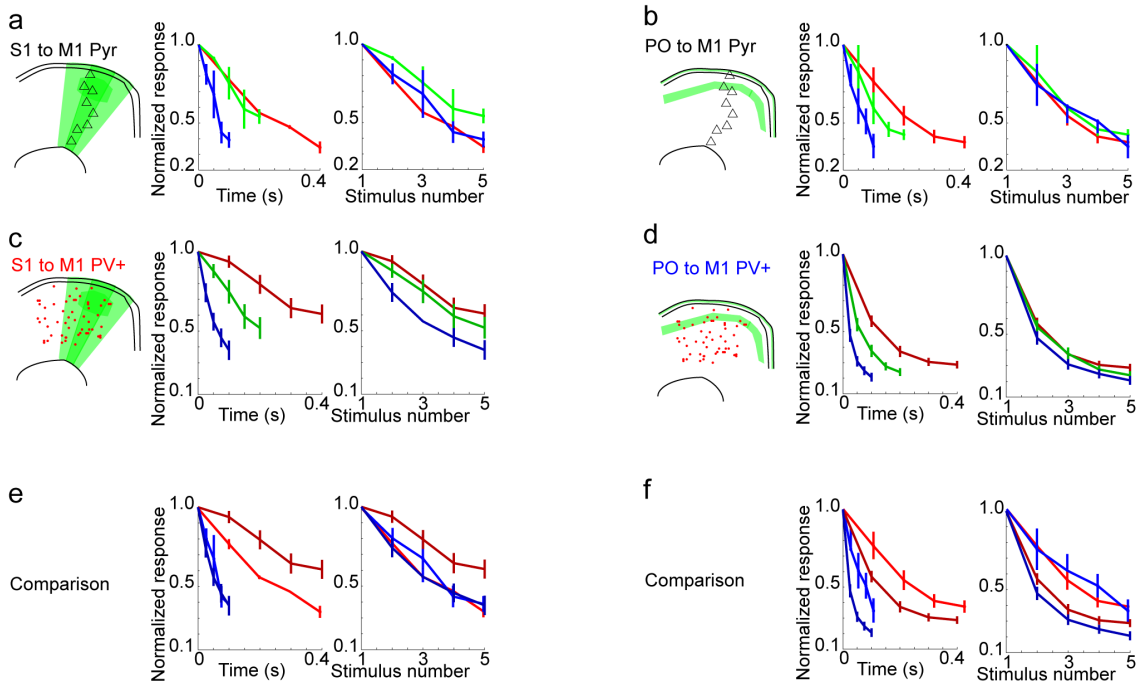

Supplemental Figure 4 | Short-term plasticity comparisons of PV+ interneurons and pyramidal neurons
(a) Short term plasticity of S1 input to pyramidal neurons. Left, normalized response to S1 stimulation at 10 Hz (red), 20 Hz (green), and 40 Hz (blue) stimulation of Chronos-GFP+. Summary graphs show responses plotted based on time of the pulses (left) or the stimulus number (right). (b) Short term plasticity of PO input to pyramidal neurons, plotted as in (a). (c,d) Short term plasticity of S1 input (c) and PO input (d) to PV+ interneurons plotted for comparison. (e,f) Comparison plot of the above data for 10Hz and 40Hz stimulation on the same axes.

675

676

677 **ACKNOWLEDGEMENTS**
678 We thank Caroline Runyan, Chinfei Chen, Nuo Li, Srivatsun Sadagopan, Taehyeon Kim, Shelby
679 Ruiz, and other members of the Hooks lab for comments and suggestions. Jay Couey
680 performed whole cell recordings contributing to the circuit mapping and short-term plasticity
681 experiments. This work was supported by a NARSAD Young Investigator Award (BMH), NIH
682 NINDS R01 NS103993 (BMH), and a CDMRP PRMRP Discovery Award PR201842 (RG and
683 BMH). The authors declare no competing financial interests or other conflict of interest.
684

685 **REFERENCES**

686 Anderson, C.T., Sheets, P.L., Kiritani, T., and Shepherd, G.M. (2010). Sublayer-specific
687 microcircuits of corticospinal and corticostriatal neurons in motor cortex. Nat Neurosci *13*, 739-
688 744.
689 Asanuma, H. (1981). Functional role of sensory inputs to the motor cortex. Progress in
690 neurobiology *16*, 241-262.
691 Atasoy, D., Aponte, Y., Su, H.H., and Sternson, S.M. (2008). A FLEX switch targets
692 Channelrhodopsin-2 to multiple cell types for imaging and long-range circuit mapping. J
693 Neurosci *28*, 7025-7030.
694 Beierlein, M., Gibson, J.R., and Connors, B.W. (2003). Two dynamically distinct inhibitory
695 networks in layer 4 of the neocortex. J Neurophysiol *90*, 2987-3000.
696 Benjamini, Y., Heller, R., and Yekutieli, D. (2009). Selective inference in complex research.
697 Philos Trans A Math Phys Eng Sci *367*, 4255-4271. 10.1098/rsta.2009.0127.
698 Blackman, A.V., Abrahamsson, T., Costa, R.P., Lalanne, T., and Sjostrom, P.J. (2013). Target-
699 cell-specific short-term plasticity in local circuits. Front Synaptic Neurosci *5*, 11.
700 10.3389/fnsyn.2013.00011.
701 Bock, D.D., Lee, W.C., Kerlin, A.M., Andermann, M.L., Hood, G., Wetzel, A.W., Yurgenson, S.,
702 Soucy, E.R., Kim, H.S., and Reid, R.C. (2011). Network anatomy and in vivo physiology of
703 visual cortical neurons. Nature *471*, 177-182. 10.1038/nature09802.
704 Braitenberg, V.B., and Schuz, A. (1998). Cortex: statistics and geometry of neuronal
705 connectivity (Springer).
706 Bruno, R.M., and Simons, D.J. (2002). Feedforward mechanisms of excitatory and inhibitory
707 cortical receptive fields. J Neurosci *22*, 10966-10975.
708 Callaway, E.M., and Luo, L. (2015). Monosynaptic Circuit Tracing with Glycoprotein-Deleted
709 Rabies Viruses. J Neurosci *35*, 8979-8985. 10.1523/JNEUROSCI.0409-15.2015.

710 Cauli, B., Audinat, E., Lambolez, B., Angulo, M.C., Ropert, N., Tsuzuki, K., Hestrin, S., and
711 Rossier, J. (1997). Molecular and physiological diversity of cortical nonpyramidal cells. J
712 Neurosci *17*, 3894-3906.
713 Chakraibarti, S., and Alloway, K.D. (2006). Differential origin of projections from SI barrel cortex
714 to the whisker representations in SII and MI. Journal of Comparative Neurology *498*, 624-636.
715 Chen, S.X., Kim, A.N., Peters, A.J., and Komiyama, T. (2015). Subtype-specific plasticity of
716 inhibitory circuits in motor cortex during motor learning. Nat Neurosci *18*, 1109-1115.
717 10.1038/nn.4049.
718 Cruikshank, S.J., Lewis, T.J., and Connors, B.W. (2007). Synaptic basis for intense
719 thalamocortical activation of feedforward inhibitory cells in neocortex. Nat Neurosci *10*, 462-468.
720 Cruikshank, S.J., Urabe, H., Nurmikko, A.V., and Connors, B.W. (2010). Pathway-specific
721 feedforward circuits between thalamus and neocortex revealed by selective optical stimulation
722 of axons. Neuron *65*, 230-245. 10.1016/j.neuron.2009.12.025.
723 Deschenes, M., Veinante, P., and Zhang, Z.W. (1998). The organization of corticothalamic
724 projections: reciprocity versus parity. Brain Res Brain Res Rev *28*, 286-308.
725 Dittrich, L., Heiss, J.E., Warrier, D.R., Perez, X.A., Quik, M., and Kilduff, T.S. (2012). Cortical
726 nNOS neurons co-express the NK1 receptor and are depolarized by Substance P in multiple
727 mammalian species. Front Neural Circuits *6*, 31. 10.3389/fncir.2012.00031.
728 Dum, R.P., and Strick, P.L. (2002). Motor areas in the frontal lobe of the primate. Physiol Behav
729 *77*, 677-682. S0031938402009290 [pii].
730 Eastwood, B.S., Hooks, B.M., Paletzki, R.F., O'Connor, N.J., Glaser, J.R., and Gerfen, C.R.
731 (2019). Whole mouse brain reconstruction and registration to a reference atlas with standard
732 histochemical processing of coronal sections. J Comp Neurol *527*, 2170-2178.
733 10.1002/cne.24602.
734 Ferezou, I., Haiss, F., Gentet, L.J., Aronoff, R., Weber, B., and Petersen, C.C. (2007).
735 Spatiotemporal dynamics of cortical sensorimotor integration in behaving mice. Neuron *56*, 907-
736 923.
737 Fino, E., Packer, A.M., and Yuste, R. (2013). The logic of inhibitory connectivity in the
738 neocortex. Neuroscientist *19*, 228-237. 10.1177/1073858412456743.
739 Fino, E., and Yuste, R. (2011). Dense inhibitory connectivity in neocortex. Neuron *69*, 1188-
740 1203. 10.1016/j.neuron.2011.02.025.
741 Gabernet, L., Jadhav, S.P., Feldman, D.E., Carandini, M., and Scanziani, M. (2005).
742 Somatosensory integration controlled by dynamic thalamocortical feed-forward inhibition.
743 Neuron *48*, 315-327.

744 Gibson, J.R., Beierlein, M., and Connors, B.W. (1999). Two networks of electrically coupled
745 inhibitory neurons in neocortex. Nature *402*, 75-79.
746 Harris, J.A., Mihalas, S., Hirokawa, K.E., Whitesell, J.D., Choi, H., Bernard, A., Bohn, P.,
747 Caldejon, S., Casal, L., Cho, A., et al. (2019). Hierarchical organization of cortical and thalamic
748 connectivity. Nature *575*, 195-202. 10.1038/s41586-019-1716-z.
749 Harris, K.D., and Shepherd, G.M. (2015). The neocortical circuit: themes and variations. Nat
750 Neurosci *18*, 170-181. 10.1038/nn.3917.
751 Harrison, T.C., and Murphy, T.H. (2014). Motor maps and the cortical control of movement. Curr
752 Opin Neurobiol *24*, 88-94. 10.1016/j.conb.2013.08.018.
753 Hatsopoulos, N.G., and Suminski, A.J. (2011). Sensing with the motor cortex. Neuron *72*, 477-
754 487. 10.1016/j.neuron.2011.10.020.
755 Hill, D.N., Curtis, J.C., Moore, J.D., and Kleinfeld, D. (2011). Primary motor cortex reports
756 efferent control of vibrissa motion on multiple timescales. Neuron *72*, 344-356.
757 10.1016/j.neuron.2011.09.020.
758 Hippenmeyer, S., Vrieseling, E., Sigrist, M., Portmann, T., Laengle, C., Ladle, D.R., and Arber,
759 S. (2005). A developmental switch in the response of DRG neurons to ETS transcription factor
760 signaling. PLoS Biol *3*, e159. 10.1371/journal.pbio.0030159.
761 Hoffer, Z.S., Hoover, J.E., and Alloway, K.D. (2003). Sensorimotor corticocortical projections
762 from rat barrel cortex have an anisotropic organization that facilitates integration of inputs from
763 whiskers in the same row. J Comp Neurol *466*, 525-544.
764 Hooks, B.M. (2017). Sensorimotor Convergence in Circuitry of the Motor Cortex. Neuroscientist
765 *23*, 251-263. 10.1177/1073858416645088.
766 Hooks, B.M., Hires, S.A., Zhang, Y.X., Huber, D., Petreanu, L., Svoboda, K., and Shepherd,
767 G.M. (2011). Laminar analysis of excitatory local circuits in vibrissal motor and sensory cortical
768 areas. PLoS Biol *9*, e1000572. 10.1371/journal.pbio.1000572.
769 Hooks, B.M., Lin, J.Y., Guo, C., and Svoboda, K. (2015). Dual-Channel Circuit Mapping Reveals
770 Sensorimotor Convergence in the Primary Motor Cortex. J Neurosci *35*, 4418-4426.
771 Hooks, B.M., Mao, T., Gutnisky, D.A., Yamawaki, N., Svoboda, K., and Shepherd, G.M. (2013).
772 Organization of cortical and thalamic input to pyramidal neurons in mouse motor cortex. J
773 Neurosci *33*, 748-760. 10.1523/JNEUROSCI.4338-12.2013.
774 Hooks, B.M., Papale, A.E., Paletzki, R.F., Feroze, M.W., Eastwood, B.S., Couey, J.J.,
775 Winnubst, J., Chandrashekar, J., and Gerfen, C.R. (2018). Topographic precision in sensory
776 and motor corticostriatal projections varies across cell type and cortical area. Nat Commun *9*,
777 3549. 10.1038/s41467-018-05780-7.

778 Huang, H., Kuzirian, M.S., Cai, X., Snyder, L.M., Cohen, J., Kaplan, D.H., and Ross, S.E.
779 (2016). Generation of a NK1R-CreER knockin mouse strain to study cells involved in Neurokinin
780 1 Receptor signaling. Genesis *54*, 593-601. 10.1002/dvg.22985.
781 Huber, D., Gutnisky, D.A., Peron, S., O'Connor, D.H., Wiegert, J.S., Tian, L., Oertner, T.G.,
782 Looger, L.L., and Svoboda, K. (2012). Multiple dynamic representations in the motor cortex
783 during sensorimotor learning. Nature *484*, 473-478. 10.1038/nature11039.
784 Isaacson, J.S., and Scanziani, M. (2011). How inhibition shapes cortical activity. Neuron *72*,
785 231-243. 10.1016/j.neuron.2011.09.027.
786 Jackman, S.L., Beneduce, B.M., Drew, I.R., and Regehr, W.G. (2014). Achieving high-
787 frequency optical control of synaptic transmission. J Neurosci *34*, 7704-7714.
788 10.1523/JNEUROSCI.4694-13.2014.
789 Jeong, M., Kim, Y., Kim, J., Ferrante, D.D., Mitra, P.P., Osten, P., and Kim, D. (2016).
790 Comparative three-dimensional connectome map of motor cortical projections in the mouse
791 brain. Sci Rep *6*, 20072. 10.1038/srep20072.
792 Kaneko, T., Caria, M.A., and Asanuma, H. (1994a). Information processing within the motor
793 cortex. I. Responses of morphologically identified motor cortical cells to stimulation of the
794 somatosensory cortex. J Comp Neurol *345*, 161-171. 10.1002/cne.903450202.
795 Kaneko, T., Caria, M.A., and Asanuma, H. (1994b). Information processing within the motor
796 cortex. II. Intracortical connections between neurons receiving somatosensory cortical input and
797 motor output neurons of the cortex. J Comp Neurol *345*, 172-184. 10.1002/cne.903450203.
798 Katzel, D., Zemelman, B.V., Buetfering, C., Wolfel, M., and Miesenbock, G. (2011). The
799 columnar and laminar organization of inhibitory connections to neocortical excitatory cells. Nat
800 Neurosci *14*, 100-107. 10.1038/nn.2687.
801 Kawaguchi, Y., and Kubota, Y. (1997). GABAergic cell subtypes and their synaptic connections
802 in rat frontal cortex. Cereb Cortex *7*, 476-486. 10.1093/cercor/7.6.476.
803 Kinnischtzke, A.K., Simons, D.J., and Fanselow, E.E. (2014). Motor cortex broadly engages
804 excitatory and inhibitory neurons in somatosensory barrel cortex. Cereb Cortex *24*, 2237-2248.
805 10.1093/cercor/bht085.
806 Kiritani, T., Wickersham, I.R., Seung, H.S., and Shepherd, G.M. (2012). Hierarchical
807 connectivity and connection-specific dynamics in the corticospinal-corticostriatal microcircuit in
808 mouse motor cortex. J Neurosci *32*, 4992-5001. 10.1523/JNEUROSCI.4759-11.2012.
809 Klapoetke, N.C., Murata, Y., Kim, S.S., Pulver, S.R., Birdsey-Benson, A., Cho, Y.K., Morimoto,
810 T.K., Chuong, A.S., Carpenter, E.J., Tian, Z., et al. (2014). Independent optical excitation of
811 distinct neural populations. Nat Methods *11*, 338-346. 10.1038/nmeth.2836.

812 Kuan, L., Li, Y., Lau, C., Feng, D., Bernard, A., Sunkin, S.M., Zeng, H., Dang, C., Hawrylycz, M.,
813 and Ng, L. (2015). Neuroinformatics of the Allen Mouse Brain Connectivity Atlas. Methods *73*, 4-
814 17. 10.1016/j.ymeth.2014.12.013.
815 Kubota, Y. (2014). Untangling GABAergic wiring in the cortical microcircuit. Curr Opin Neurobiol
816 *26*, 7-14. 10.1016/j.conb.2013.10.003.
817 Kubota, Y., Shigematsu, N., Karube, F., Sekigawa, A., Kato, S., Yamaguchi, N., Hirai, Y.,
818 Morishima, M., and Kawaguchi, Y. (2011). Selective coexpression of multiple chemical markers
819 defines discrete populations of neocortical GABAergic neurons. Cereb Cortex *21*, 1803-1817.
820 10.1093/cercor/bhq252.
821 Kuramoto, E., Furuta, T., Nakamura, K.C., Unzai, T., Hioki, H., and Kaneko, T. (2009). Two
822 types of thalamocortical projections from the motor thalamic nuclei of the rat: a single neuron-
823 tracing study using viral vectors. Cereb Cortex *19*, 2065-2077. bhn231 [pii]
824 10.1093/cercor/bhn231.
825 Kuramoto, E., Ohno, S., Furuta, T., Unzai, T., Tanaka, Y.R., Hioki, H., and Kaneko, T. (2015).
826 Ventral medial nucleus neurons send thalamocortical afferents more widely and more
827 preferentially to layer 1 than neurons of the ventral anterior-ventral lateral nuclear complex in
828 the rat. Cereb Cortex *25*, 221-235. 10.1093/cercor/bht216.
829 Lee, S., Hjerling-Leffler, J., Zagha, E., Fishell, G., and Rudy, B. (2010). The largest group of
830 superficial neocortical GABAergic interneurons expresses ionotropic serotonin receptors. J
831 Neurosci *30*, 16796-16808. 10.1523/JNEUROSCI.1869-10.2010.
832 Luo, L., Callaway, E.M., and Svoboda, K. (2018). Genetic Dissection of Neural Circuits: A
833 Decade of Progress. Neuron *98*, 865. 10.1016/j.neuron.2018.05.004.
834 Ma, Y., Hu, H., Berrebi, A.S., Mathers, P.H., and Agmon, A. (2006). Distinct subtypes of
835 somatostatin-containing neocortical interneurons revealed in transgenic mice. J Neurosci *26*,
836 5069-5082.
837 Madisen, L., Zwingman, T.A., Sunkin, S.M., Oh, S.W., Zariwala, H.A., Gu, H., Ng, L.L., Palmiter,
838 R.D., Hawrylycz, M.J., Jones, A.R., et al. (2010). A robust and high-throughput Cre reporting
839 and characterization system for the whole mouse brain. Nat Neurosci *13*, 133-140.
840 Mao, T., Kusefoglu, D., Hooks, B.M., Huber, D., Petreanu, L., and Svoboda, K. (2011). Long-
841 range neuronal circuits underlying the interaction between sensory and motor cortex. Neuron
842 *72*, 111-123. 10.1016/j.neuron.2011.07.029.
843 Marques-Smith, A., Lyngholm, D., Kaufmann, A.K., Stacey, J.A., Hoerder-Suabedissen, A.,
844 Becker, E.B., Wilson, M.C., Molnar, Z., and Butt, S.J. (2016). A Transient Translaminar

GABAergic Interneuron Circuit Connects Thalamocortical Recipient Layers in Neonatal Somatosensory Cortex. Neuron *89*, 536-549. 10.1016/j.neuron.2016.01.015.

Masamizu, Y., Tanaka, Y.R., Tanaka, Y.H., Hira, R., Ohkubo, F., Kitamura, K., Isomura, Y., Okada, T., and Matsuzaki, M. (2014). Two distinct layer-specific dynamics of cortical ensembles during learning of a motor task. Nat Neurosci *17*, 987-994. 10.1038/nn.3739.

Muñoz-Castaneda, R.Z., B.; Matho, K. S.; Wang, Q.; Chen, X.; et al. (2020). Cellular Anatomy of the Mouse Primary Motor Cortex. bioRxiv. https://doi.org/10.1101/2020.10.02.323154.

Murray, P.D., and Keller, A. (2011). Somatosensory response properties of excitatory and inhibitory neurons in rat motor cortex. J Neurophysiol *106*, 1355-1362. jn.01089.2010 [pii] 10.1152/jn.01089.2010.

Naka, A., Veit, J., Shababo, B., Chance, R.K., Risso, D., Stafford, D., Snyder, B., Egladyous, A., Chu, D., Sridharan, S., et al. (2019). Complementary networks of cortical somatostatin interneurons enforce layer specific control. Elife *8*. 10.7554/eLife.43696.

Naskar, S., Qi, J., Pereira, F., Gerfen, C.R., and Lee, S. (2021). Cell-type-specific recruitment of GABAergic interneurons in the primary somatosensory cortex by long-range inputs. Cell Rep *34*, 108774. 10.1016/j.celrep.2021.108774.

Network, B.I.C.C. (2021). A multimodal cell census and atlas of the mammalian primary motor cortex. Nature *598*, 86-102. 10.1038/s41586-021-03950-0.

Oh, S.W., Harris, J.A., Ng, L., Winslow, B., Cain, N., Mihalas, S., Wang, Q., Lau, C., Kuan, L., Henry, A.M., et al. (2014). A mesoscale connectome of the mouse brain. Nature *508*, 207-214. 10.1038/nature13186.

Ohno, S., Kuramoto, E., Furuta, T., Hioki, H., Tanaka, Y.R., Fujiyama, F., Sonomura, T., Uemura, M., Sugiyama, K., and Kaneko, T. (2012). A morphological analysis of thalamocortical axon fibers of rat posterior thalamic nuclei: a single neuron tracing study with viral vectors. Cereb Cortex *22*, 2840-2857. 10.1093/cercor/bhr356.

Packer, A.M., and Yuste, R. (2011). Dense, unspecific connectivity of neocortical parvalbumin-positive interneurons: a canonical microcircuit for inhibition? J Neurosci *31*, 13260-13271. 10.1523/JNEUROSCI.3131-11.2011.

Peters, A., and Feldman, M.L. (1976). The projection of the lateral geniculate nucleus to area 17 of the rat cerebral cortex. I. General description. J Neurocytol *5*, 63-84.

Petreanu, L., Huber, D., Sobczyk, A., and Svoboda, K. (2007). Channelrhodopsin-2-assisted circuit mapping of long-range callosal projections. Nat Neurosci *10*, 663-668.

Petreanu, L., Mao, T., Sternson, S.M., and Svoboda, K. (2009). The subcellular organization of neocortical excitatory connections. Nature *457*, 1142-1145.

879 Pfeffer, C.K., Xue, M., He, M., Huang, Z.J., and Scanziani, M. (2013). Inhibition of inhibition in
880 visual cortex: the logic of connections between molecularly distinct interneurons. Nat Neurosci
881 *16*, 1068-1076. 10.1038/nn.3446.
882 Porter, J.T., Johnson, C.K., and Agmon, A. (2001). Diverse types of interneurons generate
883 thalamus-evoked feedforward inhibition in the mouse barrel cortex. J Neurosci *21*, 2699-2710.
884 Pronneke, A., Scheuer, B., Wagener, R.J., Mock, M., Witte, M., and Staiger, J.F. (2015).
885 Characterizing VIP Neurons in the Barrel Cortex of VIPcre/tdTomato Mice Reveals Layer-
886 Specific Differences. Cereb Cortex *25*, 4854-4868. 10.1093/cercor/bhv202.
887 Reardon, T.R., Murray, A.J., Turi, G.F., Wirblich, C., Croce, K.R., Schnell, M.J., Jessell, T.M.,
888 and Losonczy, A. (2016). Rabies Virus CVS-N2c(DeltaG) Strain Enhances Retrograde Synaptic
889 Transfer and Neuronal Viability. Neuron *89*, 711-724. 10.1016/j.neuron.2016.01.004.
890 Reep, R.L., Goodwin, G.S., and Corwin, J.V. (1990). Topographic organization in the
891 corticocortical connections of medial agranular cortex in rats. J Comp Neurol *294*, 262-280.
892 10.1002/cne.902940210.
893 Rouiller, E.M., Moret, V., and Liang, F. (1993). Comparison of the connectional properties of the
894 two forelimb areas of the rat sensorimotor cortex: support for the presence of a premotor or
895 supplementary motor cortical area. Somatosens Mot Res *10*, 269-289.
896 Shepherd, G.M. (2013). Corticostriatal connectivity and its role in disease. Nat Rev Neurosci *14*,
897 278-291. 10.1038/nrn3469.
898 Shepherd, G.M., Pologruto, T.A., and Svoboda, K. (2003). Circuit analysis of experience-
899 dependent plasticity in the developing rat barrel cortex. Neuron *38*, 277-289.
900 Sherman, S.M. (2001). Tonic and burst firing: dual modes of thalamocortical relay. Trends
901 Neurosci *24*, 122-126. 10.1016/s0166-2236(00)01714-8.
902 Smith, J.B., and Alloway, K.D. (2013). Rat whisker motor cortex is subdivided into sensory-input
903 and motor-output areas. Front Neural Circuits *7*, 4. 10.3389/fncir.2013.00004.
904 Steriade, M., McCormick, D.A., and Sejnowski, T.J. (1993). Thalamocortical oscillations in the
905 sleeping and aroused brain. Science *262*, 679-685.
906 Strick, P.L., and Sterling, P. (1974). Synaptic termination of afferents from the ventrolateral
907 nucleus of the thalamus in the cat motor cortex. A light and electron microscopy study. J Comp
908 Neurol *153*, 77-106. 10.1002/cne.901530107.
909 Suter, B.A., O'Connor, T., Iyer, V., Petreanu, L.T., Hooks, B.T., Kiritani, T., Svoboda, K., and
910 G.M.G, S. (2010). Ephus: multipurpose data acquisition software for
911 neuroscience experiments. Frontiers Neurosci *4*.

912 Suter, B.A., and Shepherd, G.M. (2015). Reciprocal interareal connections to corticospinal
913 neurons in mouse M1 and S2. J Neurosci *35*, 2959-2974. 10.1523/JNEUROSCI.4287-14.2015.
914 Tan, Z., Hu, H., Huang, Z.J., and Agmon, A. (2008). Robust but delayed thalamocortical
915 activation of dendritic-targeting inhibitory interneurons. Proc Natl Acad Sci U S A *105*, 2187-
916 2192. 0710628105 [pii]
917 10.1073/pnas.0710628105.
918 Tanaka, Y.H., Tanaka, Y.R., Kondo, M., Terada, S.I., Kawaguchi, Y., and Matsuzaki, M. (2018).
919 Thalamocortical Axonal Activity in Motor Cortex Exhibits Layer-Specific Dynamics during Motor
920 Learning. Neuron *100*, 244-258 e212. 10.1016/j.neuron.2018.08.016.
921 Taniguchi, H., He, M., Wu, P., Kim, S., Paik, R., Sugino, K., Kvitsiani, D., Fu, Y., Lu, J., Lin, Y.,
922 et al. (2011). A resource of Cre driver lines for genetic targeting of GABAergic neurons in
923 cerebral cortex. Neuron *71*, 995-1013. 10.1016/j.neuron.2011.07.026.
924 Tasic, B., Yao, Z., Graybuck, L.T., Smith, K.A., Nguyen, T.N., Bertagnolli, D., Goldy, J., Garren,
925 E., Economo, M.N., Viswanathan, S., et al. (2018). Shared and distinct transcriptomic cell types
926 across neocortical areas. Nature *563*, 72-78. 10.1038/s41586-018-0654-5.
927 Tremblay, R., Lee, S., and Rudy, B. (2016). GABAergic Interneurons in the Neocortex: From
928 Cellular Properties to Circuits. Neuron *91*, 260-292. 10.1016/j.neuron.2016.06.033.
929 Tuncdemir, S.N., Wamsley, B., Stam, F.J., Osakada, F., Goulding, M., Callaway, E.M., Rudy,
930 B., and Fishell, G. (2016). Early Somatostatin Interneuron Connectivity Mediates the Maturation
931 of Deep Layer Cortical Circuits. Neuron *89*, 521-535. 10.1016/j.neuron.2015.11.020.
932 Wang, Y., Toledo-Rodriguez, M., Gupta, A., Wu, C., Silberberg, G., Luo, J., and Markram, H.
933 (2004). Anatomical, physiological and molecular properties of Martinotti cells in the
934 somatosensory cortex of the juvenile rat. J Physiol *561*, 65-90.
935 Weiler, N., Wood, L., Yu, J., Solla, S.A., and Shepherd, G.M. (2008). Top-down laminar
936 organization of the excitatory network in motor cortex. Nat Neurosci *11*, 360-366. nn2049 [pii]
937 10.1038/nn2049.
938 Wickersham, I.R., Finke, S., Conzelmann, K.K., and Callaway, E.M. (2007a). Retrograde
939 neuronal tracing with a deletion-mutant rabies virus. Nat Methods *4*, 47-49. 10.1038/nmeth999.
940 Wickersham, I.R., Lyon, D.C., Barnard, R.J., Mori, T., Finke, S., Conzelmann, K.K., Young, J.A.,
941 and Callaway, E.M. (2007b). Monosynaptic restriction of transsynaptic tracing from single,
942 genetically targeted neurons. Neuron *53*, 639-647. S0896-6273(07)00078-5 [pii]
943 10.1016/j.neuron.2007.01.033.
944 Xue, M., Atallah, B.V., and Scanziani, M. (2014). Equalizing excitation-inhibition ratios across
945 visual cortical neurons. Nature *511*, 596-600. 10.1038/nature13321.

946 Yamawaki, N., Radulovic, J., and Shepherd, G.M. (2016). A Corticocortical Circuit Directly Links
947 Retrosplenial Cortex to M2 in the Mouse. J Neurosci *36*, 9365-9374.
948 10.1523/JNEUROSCI.1099-16.2016.
949 Zeisel, A., Munoz-Manchado, A.B., Codeluppi, S., Lonnerberg, P., La Manno, G., Jureus, A.,
950 Marques, S., Munguba, H., He, L., Betsholtz, C., et al. (2015). Brain structure. Cell types in the
951 mouse cortex and hippocampus revealed by single-cell RNA-seq. Science *347*, 1138-1142.
952 10.1126/science.aaa1934.
953 Zingg, B., Hintiryan, H., Gou, L., Song, M.Y., Bay, M., Bienkowski, M.S., Foster, N.N.,
954 Yamashita, S., Bowman, I., Toga, A.W., and Dong, H.W. (2014). Neural networks of the mouse
955 neocortex. Cell *156*, 1096-1111. 10.1016/j.cell.2014.02.023.
956

957 **FIGURE LEGENDS**

958

959 **Figure 1 | Monosynaptic Retrograde Tracing of Inputs to Motor Cortex PV+ and SOM+**
960 **Neurons**

961 (a) Injection site in M1 of a SOM-Cre mouse injected with AAV-DIO-TVA-RG-EGFP (green) and
962 EnvA pseudotyped N2c RABV-tdTomato (red). Neurotrace Blue labels the tissue structure. (b)
963 tdTomato-labeled thalamic neurons (inset). (c) tdTomato+ (red) somata detected in NeuroInfo.
964 Markers are yellow. (d) Section registration in NeuroInfo. (d1) NeuroTrace Blue used as a
965 structural marker in imaged sections. (d2-d3) Current reference section (teal, d2) and brain
966 (black and white, d3) showing the reference atlas. The reference section (d2) can be aligned to
967 the current section (d1; overlaid in red in d2) by adjusting the scale, or shifting and rotating the
968 plane in which the reference brain is sectioned (control panel in e). The current plane
969 orientation for the reference brain is shown as the red box in d3 (slightly offset from coronal). A
970 nonlinear transform for each section is used to register each object in the current image to the
971 reference brain coordinates. Detected neurons (from b-c) are then transformed to the reference
972 atlas coordinate system. (e) Coronal sections showing the Allen CCF 3.0 and locations of S1
973 and motor and somatosensory thalamic nuclei (Rt, thalamic reticular nuc.; VAVL,
974 ventroanterior/ventrolateral nuc.; VM, ventromedial nuc.; VPL, ventroposterolateral nuc.; VPM,
975 ventroposteromedial nuc.). The positions of retrogradely labeled presynaptic neurons are
976 marked with a yellow dot (top image) in an example SOM-Cre mouse injected in M1.
977 Presynaptic neurons within ±0.1 mm of the plane are shown. The bottom image (e2) is labeled
978 to indicate registered thalamic areas. (f) Injection site with starter cells in a SOM-Cre mouse.
979 (f1) Merged image of green (f2) and red (f3) channels, showing yellow starter cells (white
980 arrowheads in f1-f3) and singly labeled cells (blue arrows in f1 and yellow arrows in f3). (f2)
981 Green, TVA+ neurons (putative starter cells); (f3) Red, tdTomato+ neurons (putative presynaptic
982 neurons). Right, laminar distribution of PV+ and SOM+ somata, quantified as fraction of the total
983 by layer. (g-h) Example section (g, expanded in h) showing retrograde label in S1 and thalamus
984 from M1 starter cells in a PV-Cre mouse. Note S1 label and thalamic label. (i-j) Example section
985 showing retrograde label in S1 and thalamus from M1 starter cells in a SOM-Cre mouse. Note
986 S1 label and thalamic label. (k-n) Cell detection examples in a SOM-Cre mouse. In cortex (k),
987 detected cell somata are labeled with yellow circles (l). Example images for thalamus (m-n). (o)
988 Quantification of presynaptic neuron location from brains aligned to the Allen CCF V3.0.
989 Fraction of the total presynaptic neuron population (±SEM) plotted for all M1 injections in PV-
990 Cre (N=5, red) and SOM-Cre (N=4, blue) mice. Dashed lines represent individual cases; solid

991 line represents mean. Green dashed line, threshold for testing. *, t-test p<0.05 (gray *, not
992 significant when controlling for false discovery rate) (p) Quantification of thalamic inputs for all
993 M1 injections in PV-Cre (N=5, red) and SOM-Cre (N=4, blue) mice. Data plotted as in (o),
994 subdivided into distinct thalamic nuclei.
995
996 **Figure 2 | Monosynaptic Retrograde Tracing of Inputs to PV+ and SOM+ Neurons Across**
997 **Cortical Areas**
998 (a) Schematic showing three dorsal cortical areas used for retrograde tracing from PV+ and
999 SOM+ interneurons. In PV-Cre or SOM-Cre mice, injection of AAV expressing DIO-TVA-EGFP-
1000 B19G labels potential starter cells green in a Cre-dependent manner. This vector also
1001 expressed the TVA receptor to permit rabies uptake. Subsequent injection of EnvA-
1002 pseudotyped CVS-N2c-tdTomato rabies labels starter cells yellow (red+green), at left in cartoon
1003 and labels potential presynaptic partners red (at right in many cortical and thalamic areas). (b-c)
1004 Quantification of presynaptic neuron location for injections in SOM-Cre (N=4, M2; N=4, fM1;
1005 N=4, vS1; cool colors) mice. Whole brain image stacks were aligned to the Allen CCF V3.0.
1006 Presynaptic neuronal somata were detected and coordinates in CCF assigned to brain regions.
1007 Mean fraction of the total presynaptic neuron population (±SEM) plotted as in Fig. 1.
1008 Quantification of inputs to all brain regions (b) and to thalamic nuclei (c). (d-e) Data from
1009 injections in PV-Cre (N=4, M2; N=5, fM1; N=5, vS1; hot colors) plotted as in (b-c). (f-h) Data of
1010 (b-e) replotted to compare input to SOM+ (blue) and PV+ (red) neurons in the same cortical
1011 locations: M2 (f), fM1 (g), and vS1 (h). Dotted lines represent individual cases; solid lines
1012 represent mean. Green dashed horizontal lines in b-h represent threshold for statistical
1013 comparison. Black * represent significant differences (p value as indicated) after correcting for
1014 FDR. Gray * represent comparisons not significant after correction for FDR.
1015
1016 **Figure 3 | Mapping long-range excitatory inputs to mouse motor cortex interneurons**
1017 (a) Interneurons carry feedforward inhibition in M1. Whole-cell recordings at -70 mV (blue) and
1018 0mV (red) show optically induced feedforward inhibition from S1 inputs to M1 (bottom left) with a
1019 short latency difference (inset). Difference in latency between EPSC (blue) and IPSC (red) is
1020 plotted to compare onset (mean and SE; N=29). EPSC and IPSC amplitude are roughly
1021 proportional (right) across all cortical layers (bottom right). Linear fit and 95% confidence interval
1022 (dashed lines) plotted. (b) AAV vectors expressing optogenetic activators (ChR2 or Chronos)
1023 were stereotaxically injected into cortex (S1, light green) or thalamus (PO, dark green). (c)
1024 mVenus+ axons from S1 arborize across layers of M1 in a columnar projection (left, 4x image).

1025 Fluorescence is highest in L5A (right, brightness quantified across cortical layers). (d) mVenus+
1026 axons from PO arborize across layers of M1 in two main layers (left). Fluorescence is highest in
1027 L1 and L5A (right). (e) PV-Cre mice were crossed to a tdTomato reporter (Ai14), labeling
1028 interneurons across M1 in L2-6. Postsynaptic interneurons were recorded across all layers for
1029 comparison. Inset (60x, fluorescence image, top, and corresponding brightfield image, bottom)
1030 shows patch pipette on tdTomato+ neuron in PV-Cre x Ai14 mouse. Normalized laminar
1031 distribution of PV+ somata (N=5 slices) measured at right. (f) SOM-Cre mice were crossed to a
1032 tdTomato reporter (Ai14), labeling interneurons across M1 in L2-6. L1 signal represents
1033 tdTomato+ axons from SOM+ neurons. Postsynaptic interneurons were recorded across all
1034 layers for comparison. Normalized laminar distribution of SOM+ somata (N=5 slices) measured
1035 at right. (g) Targeted whole cell recordings in brainslice were made from interneurons while
1036 stimulating with a 470nm laser at different points, shown in light blue. Full grid illustrated as in
1037 (j). (h) 470nm stimulation excites axons at example points 1 & 2, but TTX addition extinguishes
1038 responses. Addition of 4-AP permits local release at points where opsin+ axons contact
1039 interneuron dendrites (Point 1) but not distant points along the axon (Point 2). (i) Similar
1040 concentrations of 4-AP are required to restore synaptic responses regardless of postsynaptic
1041 neuron type (Pyr = pyramidal neuron). Individual cells plotted at top; average and SE plotted at
1042 bottom. Grey box represents [4-AP] used for mapping. (j) Typical input mapping experiments
1043 sampled a 12x26 point grid with points spaced at 50 mm and aligned to the pia. Brightfield
1044 image (4x) shows recording pipette in M1. (k) Heatmap shows stronger responses (red) near
1045 the soma of the recorded neuron. (l) Example traces for a L2/3 PV+ neuron show location of
1046 input. (m) Inset shows two maps to compare input between L2/3 and L5A PV+ interneurons.
1047 The summed synaptic input across the map is compared for each cell pair recorded in the same
1048 slice. Arrow indicates a point from one L2/3-L5A pair. Dashed line represents y=x (similar input
1049 to both layers); solid line represents the geometric mean of the L2/3 and L5A input strength,
1050 presented as a line of equivalent slope.
1051
1052 **Figure 4 | S1 input to M1 targets upper layer PV+ neurons**
1053 (a) Cartoon showing PV+ neurons (red) in GFP+ axons from S1. (b) S1 input to M1 PV+
1054 neurons across layers (N=58 total). Each cell is represented as a single column (vector), with
1055 the rows of the input mapped summed and aligned to the pia. Diagonal white line represents the
1056 soma location for that cell. Vertical white lines represent layer divisions. Synaptic strength
1057 (summed, in nA) for each location in depth are represented by the heatmap (scale at right).
1058 Laminar depth is normalized to 0=pia, 1=white matter. (c) Strength of synaptic input. The bar

1059 represents the geometric means of the amplitude ratio, normalized to the layer receiving the
1060 strongest input (L2/3). The overlaid graph shows the mean ratio and SD (based on 10000
1061 replicate bootstrap). Adjacent to the summary, three graphs for comparison of input strength
1062 across neurons in different cortical layers. Each point represents input to a pair of neurons in the
1063 same slice (circle for each neuron). Dashed line represents unity. N, Number of pairs; p value,
1064 Wilcoxon signed rank test. (d) Maps of synaptic input location in the dendritic arbor for PV+
1065 neurons in each layer. Top row, normalized soma-centered map (maps registered to soma
1066 center across cells). Bottom row, normalized pia-aligned maps. Normalized maps are noisy
1067 when input is weak. (e,f) Input location summarized for all four layers. Normalized mean input
1068 maps were averaged into a vector (e) and aligned to the soma (red circle). These were graphed
1069 with mean and SD (f), showing input relative to the soma in 50 mm bins. Dashed line indicates
1070 soma depth. *=p<0.05, **=p<0.01, and ***=p<0.001.
1071
1072 **Figure 5 | S1 input to M1 targets middle layer SOM+ neurons**
1073 (a) Cartoon showing SOM+ neurons (red) in GFP+ axons from S1. (b) S1 input to SOM+
1074 neurons across layers (N=53 total). Each cell is represented as a single column (vector), with
1075 the rows of the input mapped summed and aligned to the pia. Diagonal white line represents the
1076 soma location for that cell. Vertical white lines represent layer divisions. Synaptic strength
1077 (summed, in nA) for each location in depth are represented by the heatmap (scale at right).
1078 Laminar depth is normalized to 0=pia, 1=white matter. (c) Strength of synaptic input. The bar
1079 represents the geometric means of the amplitude ratio, normalized to the layer receiving the
1080 strongest input (L5A). The overlaid graph shows the mean ratio and SD (based on 10000
1081 replicate bootstrap). Adjacent to the summary, three graphs for comparison of input strength
1082 across neurons in different cortical layers. Each point represents input to a pair of neurons in the
1083 same slice (circle for each neuron). Dashed line represents unity. N, Number of pairs; p value,
1084 Wilcoxon signed rank test. (d) Maps of synaptic input location in the dendritic arbor for SOM+
1085 neurons in each layer. Top row, normalized soma-centered map (maps registered to soma
1086 center across cells). Bottom row, normalized pia-aligned maps. Normalized maps are noisy
1087 when input is weak. (e,f) Input location summarized for all four layers. Normalized mean input
1088 maps were averaged into a vector (e) and aligned to the soma (red circle). These were graphed
1089 with mean and SD (f), showing input relative to the soma in 50 mm bins. Dashed line indicates
1090 soma depth.
1091
1092 **Figure 6 | PO input to M1 PV+ neurons targets upper and middle layers**

1093 (a) Cartoon showing PV+ neurons (red) in GFP+ axons from PO. (b) PO input to PV+ neurons
1094 across layers (N=61 total). Each cell is represented as a single column (vector), with the rows of
1095 the input mapped summed and aligned to the pia. Diagonal white line represents the soma
1096 location for that cell. Vertical white lines represent layer divisions. Synaptic strength (summed,
1097 in nA) for each location in depth are represented by the heatmap (scale at right). Laminar depth
1098 is normalized to 0=pia, 1=white matter. (c) Strength of synaptic input. The bar represents the
1099 geometric means of the amplitude ratio, normalized to the layer receiving the strongest input
1100 (L5A). The overlaid graph shows the mean ratio and SD (based on 10000 replicate bootstrap).
1101 Adjacent to the summary, three graphs for comparison of input strength across neurons in
1102 different cortical layers. Each point represents input to a pair of neurons in the same slice (circle
1103 for each neuron). Dashed line represents unity. N, Number of pairs; p value, Wilcoxon signed
1104 rank test. (d) Maps of synaptic input location in the dendritic arbor for PV+ neurons in each
1105 layer. Top row, normalized soma-centered map (maps registered to soma center across cells).
1106 Bottom row, normalized pia-aligned maps. Normalized maps are noisy when input is weak. (e,f)
1107 Input location summarized for all four layers. Normalized mean input maps were averaged into a
1108 vector (e) and aligned to the soma (red circle). These were graphed with mean and SD (f),
1109 showing input relative to the soma in 50 mm bins. Dashed line indicates soma depth.
1110
1111 **Figure 7 | PO input to M1 SOM+ neurons is variable**
1112 (a) Cartoon showing SOM+ neurons (red) in GFP+ axons from PO. (b) PO input to SOM+
1113 neurons across layers (N=48 total). Each cell is represented as a single column (vector), with
1114 the rows of the input mapped summed and aligned to the pia. Diagonal white line represents the
1115 soma location for that cell. Vertical white lines represent layer divisions. Synaptic strength
1116 (summed, in nA) for each location in depth are represented by the heatmap (scale at right).
1117 Laminar depth is normalized to 0=pia, 1=white matter. (c) Strength of synaptic input. The bar
1118 represents the geometric means of the amplitude ratio, normalized to the layer receiving the
1119 strongest input (L5B). The overlaid graph shows the mean ratio and SD (based on 10000
1120 replicate bootstrap). Adjacent to the summary, three graphs for comparison of input strength
1121 across neurons in different cortical layers. Each point represents input to a pair of neurons in the
1122 same slice (circle for each neuron). Dashed line represents unity. N, Number of pairs; p value,
1123 Wilcoxon signed rank test. Plots show substantial heterogeneity. (d) Maps of synaptic input
1124 location in the dendritic arbor for SOM+ neurons in each layer. Top row, normalized soma-
1125 centered map (maps registered to soma center across cells). Bottom row, normalized pia-
1126 aligned maps. Normalized maps are noisy when input is weak. (e,f) Input location summarized

for all four layers. Normalized mean input maps were averaged into a vector (e) and aligned to the soma (red circle). These were graphed with mean and SD (f), showing input relative to the soma in 50 mm bins. Dashed line indicates soma depth.

Figure 8 | Complementary patterns of input to specific interneuron types

(a-d) Summary graphs comparing the distribution of excitatory input to PV+ and SOM+ neurons. These plots compare normalized input from (a) S1 only or (b) PO only to PV+ and SOM+ neurons. (c-d) compare input to PV+ only (c) or SOM+ only interneurons. (e) The pattern of normalized input strength to pyramidal neurons (Pyr) from S1 and PO, after Mao et al (2011) and Hooks et al. (2013). (f) Cartoon summarizing input maps. (g) Absolute input strength for S1 and PO inputs, plotted as input vectors on a log scale. From left to right, S1 input to PV+ and SOM+ neurons and PO input to PV+ and SOM+ neurons. (h) Tacr1+ neurons (a subset of SOM+ neurons) presented in a similar fashion. Left, input maps from S1 and PO. For Tacr1+ neurons, N=3/2/4/4 for S1 input to L2/3, L5A, L5B, and L6; N=3/2/9/2 for PO input. Normalized laminar distribution of Tacr1+ somata (N=4 slices) measured at right. (i) Absolute input strength averaged by layer and plotted on a log scale for comparison between S1 and PO inputs (top row) to different interneuron types. Comparison of either S! or PO input to different interneuron types presented on the same axes (bottom row).

Figure 9 | Direct comparison of synaptic and anatomical connectivity

(a) Left, absolute synaptic input strength plotted for comparison between S1 inputs to PV+ and SOM+ neurons. Right, the distribution of interneurons per layer. The weighted average input strength is shown below the graph, either as a single point (weighted avg) or the mean and SEM from N=10000 replicate (bootstrap) analysis. The ratio of input to PV/SOM is shown for each plot. (b) Comparison of anatomical input to PV+ (N=5) and SOM+ (N=4) neurons in M1 from retrograde tracing (after Fig. 1). Insets show normalized fraction of input from each case. The ratio of input to PV/SOM is shown for each plot. (c) Comparison of PV/SOM input for synaptic inputs (from S1, red; from PO, green) and for anatomical tracing (in S1, blue; in thalamus, gray). The data was resampled for N=1000 replicates to compare.

Figure 10 | Short-term plasticity at long range inputs to interneurons of mouse motor cortex

(a) Short term plasticity of S1 input to PV+ neurons. Left, example traces showing PV+ neuron response to S1 stimulation at 10 Hz (red), 20 Hz (green), and 40 Hz (blue) stimulation of

1161 Chronos-GFP+ S1 axons. Scale, 50 pA and 100 ms. Middle, average normalized traces for the
1162 same stimulus frequencies. Scale bar=1.0. Right, summary graphs showing normalized
1163 responses for 10 Hz, 20 Hz, and 40 Hz. Graphs are plotted based on time of the pulses (right)
1164 or the stimulus number (far right). (b) Short term plasticity of PO input to PV+ neurons, plotted
1165 as in (a). (c) Short term plasticity of S1 input to SOM+ neurons, plotted as in (a). (d) Short term
1166 plasticity of PO input to SOM+ neurons, plotted as in (a).
1167
1168 **Supplemental Figure 1 | Cell detection in cortex and thalamus**
1169 (a-b) Low density cortical labeling from monosynaptic rabies tracing in M1 of a SOM-Cre
1170 mouse. (a) Cells in somatosensory neocortex posterior to the injection site. (b) The same plane
1171 with cells detected. (c-d) High density cortical labeling near the injection site in M1 of a SOM-
1172 Cre mouse. (e-f) Thalamic labeling in a SOM-Cre mouse.
1173
1174 **Supplemental Figure 2 | Thalamic labeling in from SOM+ and PV+ neurons**
1175 (a-c) Retrograde labeling from fM1 SOM+ neurons. Left panel, structural stain (Neurotrace Blue)
1176 and retrogradely labeled neurons (tdTomato, red). Thalamic nuclear boundaries based on
1177 registration to CCF V3.0 atlas. Nuclei as indicated. Right panel, higher magnification version.
1178 Detected cells labeled by yellow circles. Planes shown are separated by ~0.16 mm proceeding
1179 from anterior (top, a) to posterior (bottom, c).
1180 (d-h) Retrograde labeling from M2 PV+ neurons. Left panel, structural stain (Neurotrace Blue)
1181 and retrogradely labeled neurons (tdTomato, red). Thalamic nuclear boundaries based on
1182 registration to CCF V3.0 atlas. Nuclei as indicated. Right panel, higher magnification version.
1183 Detected cells labeled by yellow circles. Planes shown are separated by ~0.16 mm proceeding
1184 from anterior (top, d) to posterior (bottom, h).
1185 PO, posterior thalamic nuc.; VAVL, ventoanterior/ventrolateral thalamic nuc.; VM, ventromedial
1186 thalamic nuc.; VPL, ventroposteriolateral thalamic nuc.; VPM, ventroposteriomedial thalamic
1187 nuc.
1188
1189 **Supplemental Figure 3 | Consistency of monosynaptic retrograde tracing**
1190 (a-b) Quantification of presynaptic neuron location in the whole brain (a) and thalamus (b)
1191 plotted as bar graphs to emphasize differences between individual retrograde tracing cases. For
1192 SOM-Cre (N=4, blue) mice, the fraction of the total presynaptic neuron population (±SEM)
1193 plotted for all M1 injections. Bars represent individual cases. (c-d) Quantification of presynaptic

1194 neuron location in the whole brain (a) and thalamus (b) for PV-Cre (N=5, rec) mice, plotted as
1195 above.
1196
1197 **Supplemental Figure 4 | Short-term plasticity comparisons of PV+ interneurons and**
1198 **pyramidal neurons**
1199 (a) Short term plasticity of S1 input to pyramidal neurons. Left, normalized response to S1
1200 stimulation at 10 Hz (red), 20 Hz (green), and 40 Hz (blue) stimulation of Chronos-GFP+.
1201 Summary graphs show responses plotted based on time of the pulses (left) or the stimulus
1202 number (right). (b) Short term plasticity of PO input to pyramidal neurons, plotted as in (a). (c,d)
1203 Short term plasticity of S1 input (c) and PO input (d) to PV+ interneurons plotted for comparison.
1204 (e,f) Comparison plot of the above data for 10Hz and 40Hz stimulation on the same axes.
1205